1 Redistribution of cholesterol from vesicle to plasmalemma

2 controls fusion pore geometry

3 Boštjan Rituper,[1] Alenka Guček,[1,10] Marjeta Lisjak,[1] Urszula Gorska,[1,11]

4 Aleksandra Šakanović,[2] Saša Trkov Bobnar,[1,3] Eva Lasič,[1] Mićo Božić,[1]

5 Prabhodh S. Abbineni,[4] Jernej Jorgačevski,[1,3] Marko Kreft,[1,3] Alexei

6 Verkhratsky,[3,5,6] Frances M. Platt,[7] Gregor Anderluh,[2] Matjaž Stenovec,[1,3]

7 Bojan Božič,[8] Jens R. Coorssen,[9] Robert Zorec[1,3,12,]*

8 [1]Laboratory of Neuroendocrinology-Molecular Cell Physiology, Institute of Pathophysiology,

9 University of Ljubljana, Faculty of Medicine, Ljubljana, Slovenia

10 [2]Celica Biomedical, 1000, Ljubljana, Slovenia

11 [3]Laboratory for Molecular Biology and Nanobiotechnology, National Institute of Chemistry,

12 Ljubljana, Slovenia

13 [4]Department of Pharmacology, University of Michigan, Ann Arbor, MI 48109-5632, USA

14 [5]Faculty of Biology, Medicine and Health, The University of Manchester, Manchester, M13 9PT, UK

15 [6]Achucarro Center for Neuroscience, IKERBASQUE, 48011 Bilbao, Spain

16 [7]Department of Pharmacology, University of Oxford, Oxford, OX1 3QT, UK

17 [8]Institute of Biophysics, Faculty of Medicine, University of Ljubljana, Slovenia

18 [9]Department of Health Sciences, Faculty of Applied Health Sciences and Department of Biological

19 Sciences, Faculty of Mathematics & Science, Brock University, St Catherine's, Ontario, Canada

20 [10]Present address: Department of Medical Cell Biology, Uppsala University, Uppsala, Sweden

21 [11]Present address: Smoluchowski Institute of Physics, Jagiellonian University, Krakow,

22 Poland

23   [12]Lead Contact

24   *Correspondence: robert.zorec@mf.uni-lj.si

25   Graphical Abstract
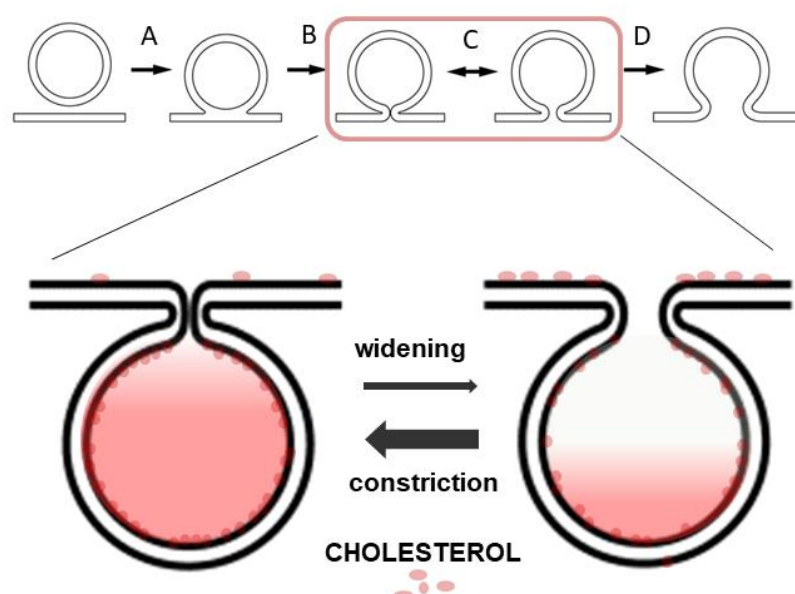
26
27   Top: stages through which a vesicle interacts with the plasmalemma. Stage A denotes hemifusion,

28   which proceeds to stage B, with a narrow fusion pore, which can then reversibly open (stage C),

29   before widening fully (stage D). Bottom: redistribution of cholesterol from the vesicle to the outer

30   leaflet of the plasmalemma controls fusion pore constriction.

31   In Brief

32   A membrane pore is formed when the vesicle membrane fuses with the plasmalemma. Proteins were

33   considered key regulators of the opening and closing of this fusion pore. Here, evidence is provided to

34   show that cholesterol, a membrane constituent, determines a radial force constricting the fusion pore,

35   revealing that the fusion pore functions as a proteolipidic structure.

36   Highlights

37   •   Intravesicular cholesterol redistributes to the outer leaflet of the plasmalemma.

38 • Cholesterol depletion widens the fusion pore, whereas cholesterol enrichment constricts the fusion

39   pore.

40 • A model of cholesterol-dependent force preventing fusion pore widening is developed.

41 • Disease-related increase in vesicle cholesterol constricts the fusion pore.

42 ABSTRACT

43 Eukaryotic vesicles fuse with the plasmalemma to form the fusion pore, previously considered to be

44 unstable with widening of the pore diameter. Recent studies established that the pore diameter is

45 stable, reflecting balanced forces of widening and closure. Proteins are considered key regulators of

46 the fusion pore, whereas the role of membrane lipids remains unclear. Super-resolution microscopy

47 revealed that lactotroph secretory vesicles discharge cholesterol after stimulation of exocytosis;

48 subsequently, vesicle cholesterol redistributes to the outer leaflet of the plasmalemma. Cholesterol

49 depletion in lactotrophs and astrocytes evokes release of vesicle hormone, indicating that cholesterol

50 constricts the fusion pore. A new model of cholesterol-dependent fusion pore diameter regulation is

51 proposed. High-resolution measurements of fusion pore conductance confirmed that the fusion pore

52 widens with cholesterol depletion and constricts with cholesterol enrichment. In fibroblasts lacking

53 the Npc1 protein, in which cholesterol accumulates in vesicles, the fusion pore is narrower than in

54 controls, showing that cholesterol regulates fusion pore geometry.

55 INTRODUCTION

56 Membrane fusion, fundamental to the life of eukaryotic cells, contributes to diverse processes,

57 including catabolic and biosynthetic pathways, as well as to vesicle-based secretion (Brose et al.,

58 2019). Regulated exocytosis, which proceeds through a merger between the vesicle membrane and the

59 plasmalemma (PM), leads to the formation of a fusion pore, through which molecules stored in the

60 vesicle lumen, including hormones and neurotransmitters, exit into the extracellular space (Sharma

61 and Lindau, 2018). The views that emerged decades ago (Rand and Parsegian, 1986), assumed that

62 once the fusion pore forms, the vesicle membrane integrates abruptly and fully with the PM (full

63 exocytosis). However, recent studies have postulated that the open fusion pore may close again after a

64 while (transient or reversible exocytosis). The stages that a vesicle undergoes during exocytosis were

65 confirmed by measurements of discrete steps in membrane capacitance (C_m), which is linearly related

66 to the membrane area, and is affected by vesicle fusion and fission (Neher and Marty, 1982).

67 Advancements through the stages of vesicle-PM fusion appear to depend on vesicle size (Flasker et

68   al., 2013; Jorgacevski et al., 2010; Shin et al., 2018). In synaptic communication, that is specialized

69   for fast signaling, vesicles with relatively small diameters predominantly undergo full exocytosis

70   (Grabner and Moser, 2018; He et al., 2006; Klyachko and Jackson, 2002). The fusion pore opening

71   follows the calcium trigger by a millisecond and is considered to be driven by the soluble N-

72   ethylmaleimide-sensitive factor attachment protein receptors (SNAREs), a protein complex

73   responsible for facilitating exocytotic membrane fusion (Brose et al., 2019).

74   The structure of the fusion pore walls is still debated, although it is widely considered to be

75   proteolipidic in nature (Sharma and Lindau, 2018).Therefore, it is likely that both proteins and lipid

76   membrane molecules affect the fusion pore, including stabilizing its structure. In this study, we

77   examined whether cholesterol, the most common steroid in humans and a major constituent of the cell

78   membrane, affects fusion pore geometry. To this end, we monitored single-vesicle cargo discharge

79   and characterized unitary exocytotic events by measuring changes in C_m (Akerman et al., 1991;

80   Mason et al., 1988; Neher and Marty, 1982; Sikdar et al., 1989; Zorec et al., 1991). Previous studies

81   indicated that cholesterol may regulate exocytosis, most likely by affecting the local curvature of the

82   membrane to promote merger of the apposed monolayers (Churchward and Coorssen, 2009;

83   Churchward et al., 2005a; Cookson et al., 2013; Rituper et al., 2013a; Rituper et al., 2012; Wang et

84   al., 2010). Another study demonstrated that cholesterol facilitates spontaneous and inhibits evoked

85   synaptic secretion (Wasser et al., 2007). In endocrine pituitary cells, cholesterol appears to be

86   necessary for the fusion of vesicle and plasma membranes (Rituper et al., 2013a; Rituper et al., 2012),

87   whereas in insulin-secreting cells, excess cholesterol inhibits vesicle exocytosis (Xu et al., 2017).

88   These contradictory results may arise from cholesterol acting differently at various stages of vesicle

89   interactions with the PM.

90   Using a cholesterol marker (Lasic et al., 2019; Skocaj et al., 2014), we found that during stimulated

91   exocytosis, vesicle cholesterol mixes with the PM of the outer leaflet; this occurs by cholesterol

92   transfer through the fusion pore, likely driven by the cholesterol concentration gradient between these

93   two membrane compartments. Here, depleting cholesterol by exposing cells to methyl-β-cyclodextrin

94   (MβCD) stimulated vesicle cargo release independently of cytosolic Ca^{2+}, indicating that cholesterol

4

95   may contribute to the constriction of the fusion pore. We propose a model of cholesterol-dependent

96   radial force that regulates the fusion pore diameter. High-resolution measurements of C_m and fusion

97   pore conductance (G_p), which reports the electrical geometry of the fusion pore, confirmed our

98   theoretical predictions that cholesterol depletion widens and cholesterol enrichment constricts the

99   fusion pore. Consistent with this hypothesis, cholesterol-rich vesicles in fibroblasts lacking the

100   Niemann-Pick Type C1 (Npc1) protein, a cellular model of the lysosomal storage disease Niemann-

101   Pick disease Type C1 (NPC), exhibited a narrower fusion pore than wild-type controls. Our findings

102   provide a conceptual advancement of our understanding of membrane fusion pores.

RESULTS

103

Secretory Vesicles Contain Cholesterol

104

105   Lactotroph vesicles store and secrete prolactin (PRL). We labeled these cells by anti-PRL antibodies

106   (Figure 1A) together with fluorescent (TopFluor) cholesterol (Figure 1B), which has similar

107   properties to native cholesterol (Holtta-Vuori et al., 2008), to determine whether PRL and cholesterol

108   are stored in the same vesicles. The exposure of cells to TopFluor for minutes predominantly labeled

109   the PM (Rituper et al., 2013a). Longer exposure, that ended with a 2 min wash of cells with MβCD to

110   remove background fluorescence (see STAR Methods), led to most vesicles containing both markers

111   (Figure 1C). Diameters of structures with both markers (Figures 1D–1F) were determined by

112   constructing intensity profiles of labeled structures, fitting Gaussian curves and measuring full width

113   at half maximum (FWHM = $2\sigma(2\ln2)^{1/2}$, where σ denotes standard deviation) (Figure 1C, inset). The

114   PRL- and TopFluor-positive structures (n = 384, from ten cells) were of similar diameter: 249 ± 2 nm

115   (Figure 1D) and 243 ± 3 nm (Figure 1E), respectively. Fitting the pairs of PRL- and TopFluor-

116   positive vesicle diameters by linear regression yielded a slope of k = 0.98 ± 0.01 (correlation

117   coefficient r = 0.84, $p < 0.001$, n = 384; Figure 1F), indicating that cholesterol may be present in PRL-

118   containing secretory vesicles, consistent with previous observations (Bogan et al., 2012). This

119   suggests that stimulation of regulated exocytosis may instigate the transfer of vesicle cholesterol, thus

120   affecting the composition of cholesterol in the PM.

5

121   ## Stimulation of Regulated Exocytosis Reduces the Density and Size of

122   ## Cholesterol-Rich PM Domains

123   To test how stimulated exocytosis affects cholesterol-rich PM domains, we first used a cholesterol-

124   specific marker, mCherry-D4-PFO (D4) (Lasic et al., 2019; Maekawa, 2017; Ohno-Iwashita et al.,

125   1990; Skocaj et al., 2014), to visualize the cholesterol content in the PM, which is rich in cholesterol

126   in pituitary cells (Rituper et al., 2013a). Cells were exposed to D4, washed subsequently with

127   extracellular solution (vehicle, protocol A, Table S1), and finally fixed with 2% formaldehyde. The

128   D4 labelled the PM (Figure 2A). Neither intracellular injection of the D4 peptide nor transfection of

129   cells with the mCherry-D4-encoding plasmid produced significant labeling of the cytoplasmic leaflet

130   of the PM (Figure S1). In MβCD-treated (10 mM, 30 min) cells (Najafinobar et al., 2016; Rituper et

131   al., 2013a), the PM D4 staining was strongly reduced (Figure 2B, right), indicating, together with the

132   results in Figure S1, that D4 associates with the cholesterol-rich domains in the outer PM leaflet. The

133   extent of D4 labeling was determined by delineating a band overlaying the PM (Figure S2) and

134   calculating the percentage of D4-positive pixels, relative to all the pixels in the region of interest.

135   MβCD reduced the extent of D4 labeling from 9.0% ± 0.5% in controls to 2.1% ± 0.3% in MβCD-

136   treated cells ($p < 0.001$, n = 50 optical slices from five cells per group). This is consistent with the

137   biochemically determined cholesterol content (Amplex Red, see STAR Methods) of MβCD-treated

138   pituitary cells, which was 56.8% ± 10.6%, normalized to controls; a similar reduction to 52.3% ±

139   4.9% was also obtained in astrocytes (Table S2). MβCD selectively extracted cholesterol from cells

140   without affecting other membrane lipids, as quantified by high-performance thin layer

141   chromatography (Table S2).

142   Second, we tested whether the distribution of cholesterol in the PM was affected by regulated

143   exocytosis. D4-labeled cells were depolarized with extracellular solution containing 50 mM KCl,

144   which triggers exocytotic secretion (Stenovec et al., 2004); and were subsequently examined by

145   microscopy (Table S1, protocol B). D4-labeling of the PM was reduced in the stimulated cells

146   (Figures 2C and 2D). As the decrease in the signal depends on the noise level, we assessed the

6

147   changes in D4 area at several intensity thresholds (middle and bottom panels, Figures 2C and 2D).

148   The D4-labeled pixels above the threshold were similarly significantly reduced in exocytosis-

149   stimulated cells (Figure 2E; n = 30 optical slices, five cells), indicating that the D4-unlabeled

150   cholesterol delivered from vesicles diluted the D4-labeled cholesterol in the PM. By readjusting the

151   acquisition parameters for faint signals, we further tested the density reduction of D4-positive

152   domains after stimulation of exocytosis ($p < 0.001$, Figures S3A and S3B), and also determined that

153   the size of individual D4 domains (insets in Figures 2C and 2D) decreased after stimulation of

154   regulated exocytosis ($p < 0.05$, Figures S3C and S3D).

155   These data indicate that stimulation of regulated exocytosis leads to changes in cholesterol

156   distribution in the external leaflet of the PM.

157

158   Vesicle Cholesterol Delivery to the PM Correlates with Exocytotic Release of

159   Prolactin

160   To further examine whether regulated exocytosis initiates cholesterol redistribution to the PM, we

161   performed three sets of experiments using distinct labeling approaches (protocols C, D, and E; Table

162   S1).

163   First, cholesterol-rich domains were labeled with D4 and PRL at the PM surface with antibodies

164   (Figures 3A and 3B). In controls (REST), protocol C (Table S1) was used to label vesicle-stored PRL

165   and cholesterol-rich domains in non-stimulated cells; protocol D (Table S1) was used to label surface-

166   deposited PRL granules in stimulated cells, and cholesterol-rich domains were labeled before

167   stimulation of exocytosis.

168   Next, we assessed the degree of association between both markers. Insets (Figure 3C; arrows) indicate

169   the types of associations between PRL- and D4-positive structures at the PM; some are overlapping or

170   in contact (i.e., are associated) and others are separated (not associated). The distance between the

7

171   non-associated structures was quantified (Figures S2C and S2D), revealing that depolarization-

172   induced exocytosis significantly increased the D4-PRL distance (Figure 3D) from 0.28 ± 0.03 μm

173   (REST, n = 182; nine cells) to 0.75 ± 0.13 μm (STIM, n = 96; ten cells, $p < 0.001$; see also Figure

174   S2). Stimulation of exocytosis also significantly decreased the percentage of D4-PRL associations, as

175   the overlap of D4- and PRL-positive structures at the PM decreased (Figure 3E) from $54.9\% \pm 2.0\%$

176   in controls (REST, n = 9 cells) to $39.6\% \pm 2.5\%$ in exocytosis-stimulated cells (STIM, n = 24 cells, p

177   < 0.01). The decrease in the D4-PRL association in both experiments most likely reflects delivery of

178   unlabeled vesicle-stored cholesterol to the PM during stimulated exocytosis.

179   To quantify the putative vesicle-stored cholesterol delivery, we modified the labeling protocol D by

180   adding D4 to the exocytosis-stimulating solution (see Table S1, protocol E) to visualize the

181   exocytosis-delivered cholesterol (Figure 3C [STIM + D4]). The degree of D4-PRL association was

182   significantly higher in this group of cells (Figure 3E, red column, STIM + D4, $61.1\% \pm 3.2\%$, n = 16

183   cells) versus STIM ($39.6\% \pm 2.5\%$, n = 24 cells, $p < 0.01$). Moreover, the D4-positive PM area

184   (relative to the total PM area) was also significantly higher in the STIM + D4 group (Figure 3F; 9.9%

185     $\pm 0.5\%$, n = 16 cells) versus the STIM group ($7.7\% \pm 1.0\%$, n = 14 cells, $p < 0.05$).

186   To further test the delivery of vesicle cholesterol to the PM, the labeling protocols E and F (Table S1)

187   were used, whereby the cholesterol-rich domains were first exposed to D4 (red fluorescence) to

188   saturate the cholesterol-rich sites. Subsequently, we used a green fluorescent peptide, EGFP-D4, to

189   visualize the newly added cholesterol after washing with vehicle (controls, REST) or stimulating

190   exocytosis with 50 mM KCl (STIM, Figure 3G). In this experiment, the D4-positive pre-labeled (red)

191   membrane area significantly decreased (Figure 3H) from $7.0\% \pm 0.5\%$ in controls (REST, red bar, n =

192   20 cells) to $3.8\% \pm 1.6\%$ in exocytosis-stimulated cells (STIM, red bar, n = 19 cells, $p < 0.001$).

193   However, the green fluorescent EGFP-D4 PM area increased significantly from $1.2\% \pm 0.1\%$ in

194   controls (REST, green bar, n = 20 cells) to $1.6\% \pm 0.1 \%$ in stimulated cells (STIM, green bar, n =19

195   cells, $p < 0.01$).

196   These data confirmed that vesicle cholesterol is delivered to the PM in the process of exocytosis,

197   likely along the gradient between vesicle-stored and PM cholesterol.

8

198   Exocytotic Release from Lactotrophs and Astrocytes is Stimulated by

199   Cholesterol Extraction with MβCD

200   Exposing cells to 10 mM MβCD for 30 min reduced membrane cholesterol levels (Figure 2B) without

201   affecting other membrane lipids (Table S2), consistent with previous reports (Churchward and

202   Coorssen, 2009; Rituper et al., 2012). Next, we probed whether cholesterol extraction with MβCD

203   affects exocytotic release in two physiologically distinct cell types: electrically excitable lactotrophs

204   and electrically non-excitable astrocytes.

205   Application of MβCD to lactotrophs significantly increased the cumulative release of PRL over a

206   period of 30 min (Figure 4A) from 0.54 ± 0.15 ng/mL in controls (REST) to 2.48 ± 0.10 ng/mL in

207   treated cells (+MβCD, $p < 0.01$; n = 4 ELISA reactions). In astrocytes expressing ANP.emd peptide,

208   which accumulates in secretory vesicles and can be released from cells by regulated exocytosis

209   (Stenovec et al., 2014; Trkov et al., 2012), MβCD treatment (10 mM, 30 min) also increased the

210   release of ANP.emd (Figure 4B), measured as changes in the bath fluorescence relative to the control.

211   Assuming a linear relationship between the bath fluorescence intensity change and ANP.emd release,

212   MβCD treatment triggered on average 26% more ANP.emd release compared with controls. MβCD

213   treatment did not cause any significant cell death within the relevant time interval, indicating that cell

214   lysis did not contribute to an increase in signal fluorescence.

215   To validate these results at the single-cell level, we first imaged secreted PRL-containing granular

216   content on the cell surface of lactotrophs (Cochilla et al., 1999; Mason et al., 1988) and the non-

217   secreted, cytoplasmic, PRL-containing vesicles (Figures 4C–4F). During 30-min exposure to MβCD,

218   the normalized number of PM surface-attached PRL granules significantly increased (Figure 4D)

219   from 0.016 ± 0.003 granules/μm^3 in controls (REST, n = 13 cells) to 0.103 ± 0.016 granules/μm^3 in

220   treated cells (+MβCD, n = 16 cells, $p < 0.01$). Similarly, exposure to MβCD decreased the quantity of

221   cytoplasmic PRL-loaded vesicles in lactotrophs, indicating a substantial stimulation of vesicle cargo

222   discharge during cholesterol extraction (Figure 4F). The surface area of above-threshold pixels

223   (denoting cytoplasmic PRL vesicles; Figure 4G), relative to all pixels in the cell, significantly

9

224   decreased (Figure 4H) from 10.4% ± 0.9% in controls (REST, n =16 cells) to 3.6% ± 1.0% in treated

225   cells (+MβCD, n = 16 cells, $p < 0.001$).

226   MβCD treatment of astrocytes did not significantly change the above-threshold vesicular nucleotide

227   transporter (VNUT) signal that represent ATP-containing vesicles (Gundersen et al., 2015) (Figure

228   4L, top graph), nor the above-threshold vesicle glutamate transporter 1 (VGLUT1) signal that

229   represents glutamate-containing vesicles (Stenovec et al., 2008) (Figure 4L, top graph). However, we

230   observed significantly less VNUT- and VGLUT1-positive vesicles in the 2-µm-thick band region,

231   adjacent to the PM (Figure 4L, bottom graph). In this region, MβCD treatment significantly decreased

232   the level of above-threshold VNUT-positive pixels from 0.38% ± 0.05% in controls (VNUT, REST,

233   n=19 cells) to 0.21% ± 0.04% in treated cells (VNUT, +MβCD, n = 23 cells, $p < 0.01$) as well as the

234   amount of above-threshold VGLUT1-positive pixels from 0.17% ± 0.02% in controls (VGLUT1,

235   REST, n = 19 cells) to 0.11% ± 0.01% in treated cells (VGLUT1, +MβCD, n = 23 cells, $p < 0.05$).

236   These results demonstrate that MβCD-induced cholesterol extraction facilitates exocytotic release

237   from both of the cell types studied.

238   **The Cholesterol Extraction-Mediated Increase in Vesicle Release is**

239   **Independent of Changes in Cytosolic Free Ca^{2+} Levels**

240   It is conceivable that MβCD cell treatment enhances the observed exocytotic release through an

241   unspecific increase in cytosolic free Ca^{2+} concentration ($[Ca^{2+}]_i$), a stimulus for regulated exocytosis

242   in both cell types (Kreft et al., 2004; Krzan et al., 2003; Zorec et al., 1991). Therefore, we measured

243   the changes in $[Ca^{2+}]_i$ in lactotrophs and astrocytes during the exposure to 10 mM MβCD or 10 mM

244   cholesterol-replenishing solution. During MβCD treatment $[Ca^{2+}]_i$ increased in lactotrophs but

245   decreased in astrocytes (Figure S4). Therefore, these results indicate that cholesterol depletion may

246   promote the discharge of vesicle in a $[Ca^{2+}]_i$-independent manner by affecting the fusion pore

247   diameter.

A Theoretical Description of Cholesterol-Mediated Fusion Pore Properties

248

249   We developed a model that describes the mechanism of cholesterol redistribution between the vesicle

250   and the PM along a cholesterol gradient, passing through the highly curved membranous fusion pore

251   (Figures 5A and 5B). At the fusion pore orifice, a shift in the membrane curvature occurs, from a

252   negative curvature in the luminal face of the vesicle membrane to a positive one at the fusion pore

253   orifice. The change in the curvature affects the properties of the PM (Yesylevskyy et al., 2017),

254   forming a boundary for membrane molecules with negative spontaneous curvature, such as

255   cholesterol, to be transferred from the vesicle membrane to the PM. This generates tension (Baumgart

256   et al., 2003; Julicher and Lipowsky, 1996) and creates a radial force, constricting the fusion pore

257   diameter (Figure 5C). As the fusion pore diameter at steady state depends on the vesicle diameter

258   (Flasker et al., 2013; Jorgacevski et al., 2010; Shin et al., 2018), this model also considers this

259   relationship (Figure 5D). Details of how this model was developed are provided in the Supplemental

260   Information (Figure S6).

261   In brief, line tension at the fusion pore, creating a radial force constricting the fusion pore diameter

262   (Figure 5C; Supplemental Information, eq. 5), is proportional to the difference in cholesterol

263   concentrations between the vesicle membrane and the PM (Supplemental Information, eq. 6). Due to

264   its anisotropic and negative spontaneous curvature, cholesterol determines the bending elasticity of

265   the membrane and preferentially accumulates in membrane domains with relatively high local

266   negative curvature (Chen and Rand, 1997; Jorgacevski et al., 2010). Therefore, the cholesterol

267   density in the membrane is larger at more negatively curved membranes (Yesylevskyy et al., 2017),

268   i.e. at smaller fusion pore radii with respect to the secretory vesicle size (Supplemental Information,

269   eq. 7). By simulating the influence of the difference in cholesterol concentrations between the vesicle

270   membrane and the PM, we found a linear dependence of fusion pore radius on vesicle radius (Figure

271   5D; Supplemental Information, eq. 9), where the slope of this relationship is determined by

272   cholesterol-related parameters (Supplemental Information). Increased versus reduced cholesterol

273 content is predicted to result in a relatively narrow versus wide fusion pore radius, respectively

274 (Figure 5D).

Fusion Pore Conductance Increases in Cholesterol-Depleted Lactotrophs and Astrocytes

277 To verify the role of cholesterol in determining the vesicle fusion pore properties (Figure 5), unitary

278 exocytotic events were monitored by high-resolution membrane capacitance (C_m) measurements in

279 lactotrophs and astrocytes under control, cholesterol-depleted, and cholesterol-replenished conditions

280 (Table S3).

281 In controls, ~64% of patch-clamped lactotrophs (52 of 81) exhibited upward steps in C_m, and 95% (n

282 = 1354) of those were reversible, meaning that a discrete upward step in C_m was followed by a

283 downward step of similar amplitude within 3 s (Gucek et al., 2016) (Figure 6A). Similar reversible

284 events were observed in astrocytes (Figure 6B). These consecutive steps in C_m reflect transient

285 exocytotic fusion pore openings (Alvarez de Toledo et al., 1993; Zorec et al., 1991), whereas

286 irreversible upward steps in C_m (i.e. full fusion, Figure 6A) represent a complete merger of the vesicle

287 membrane with the PM (Neher and Marty, 1982). Similar to a previous study (Rituper et al., 2012),

288 the 10 mM MβCD pretreatment (Table S2) decreased the frequency of reversible fusion pore opening

289 events (Figure 6C, Table S3). In cholesterol-replenished cells, the frequency of reversible fusion pore

290 events was significantly increased, whereas full fusion events decreased. Moreover, the frequency of

291 irreversible events was not affected by cholesterol depletion in lactotrophs; however, after cholesterol

292 replenishment, the frequency of irreversible events decreased slightly (Table S3).

293 The probability of observing a fusion pore in the open state, calculated as the sum of all dwell times

294 of reversible C_m events divided by the time of the recording, decreased significantly after cholesterol

295 depletion ($p < 0.01$; Figure 6E) and was partially, yet significantly, restored after cholesterol

296 replenishment to 0.86% ($p < 0.01$ versus control; Table S3). The fusion pore conductance (G_p), a

297 measure of the fusion pore diameter, can be calculated for transient, i.e. reversible C_m events that

12

298   display a projection from the imaginary (Im) to the real (Re) part of the admittance signal (Lollike et

299   al., 1995). Such C_m events comprised 15% of all events in control (203 of 1354 events), 11% in

300   cholesterol-depleted cells (44 of 400 events), and 28% in cholesterol-replenished cells (249 of 877

301   events; Figure 6G). The settings of our experimental system allowed the detection of fairly narrow

302   diameter fusion pores (0.3–3 nm) (Jorgacevski et al., 2010); therefore, the decrease in the relative

303   occurrence of projected C_m events in MβCD-treated cells indicated that cholesterol extraction

304   promoted the formation of fusion pores with wider diameters, which were no longer detectable as a

305   projection between the Im and Re parts of the admittance signals. Consistent with this, the G_p/C_v ratio,

306   in which the fusion pore conductance (G_p) is normalized to the vesicle size (C_v), significantly

307   increased in cholesterol-depleted cells (Figure 6G, $p < 0.05$; Table S3). In cholesterol-replenished

308   lactotrophs, the G_p/C_v ratio decreased significantly in comparison with controls ($p < 0.01$; Table S3).

309   The cholesterol-mediated changes in G_p/C_v correlated with the measured cholesterol concentration

310   (Table S2 and Figure 6I).

311   Similar results were obtained in astrocytes. The frequency of reversible C_m events significantly ($p <$

312   0.01) decreased in MβCD-treated cells and was restored ($p < 0.01$) in cholesterol-replenished cells

313   (Figure 6D). Unlike in lactotrophs, we observed a significant decrease in the frequency of irreversible

314   events in cholesterol-depleted astrocytes, which was restored by cholesterol replenishment. The

315   percentage of reversible events, in comparison with all events, decreased in cholesterol-depleted

316   astrocytes and was restored by cholesterol replenishment (Table S3).

317   The probability of observing the fusion pore open state (Figure 6F) was significantly reduced by

318   cholesterol depletion ($p < 0.01$; Table S3). Cholesterol replenishment fully restored the open fusion

319   pore probability ($p < 0.01$ versus cholesterol-depleted cells; Table S3). Similar to recordings in

320   lactotrophs, there was a decrease of reversible events with projections (representing relatively narrow

321   fusion pore diameters) from the Im to Re parts of the admittance (Lollike et al., 1995), from 43% (249

322   of 576 events) in controls to 25% (31 of 122 events) in cholesterol-depleted astrocytes; this increased

323   to 29% (132 of 462 events) with cholesterol replenishment. Accordingly, the G_p/C_v ratio (Figure 6H)

324   in astrocytes increased significantly after cholesterol depletion ($p < 0.01$) and was fully restored by

13

325   cholesterol replenishment ($p < 0.01$ versus cholesterol-depleted cells; Table S3). The cholesterol-

326   dependent G_p/C_v correlated with the measured cholesterol (Figure 6J).

327   These results demonstrate that relatively high cholesterol levels constrict fusion pores, whereas

328   cholesterol depletion widens fusion pores, consistent with our theoretical predictions (Figure 5D) as

329   further established in Figure S5, which display the relationship between the fusion pore diameter

330   (estimated from G_p) and the vesicle diameter (determined from C_v) (lines fitted to eq. 9: Supplemental

331   Information).

Reduced Fusion Pore Conductance (G_p) in Cholesterol-Enriched Vesicles of Niemann-Pick Disease Type C1 Null Mouse Fibroblasts

334   The fibroblast cell model of lysosomal storage disease, in which the Npc1 protein, the vesicle

335   cholesterol transporter, is deleted, demonstrates an accumulation of cholesterol in the vesicle lumen

336   and membrane (Liscum, 2000; Mukherjee and Maxfield, 2004). Confocal microscopy of fixed

337   cultured cells revealed abundant D4-positive vesicles in the cytoplasm of $Npc1^{-/-}$ cells (Figures 7A

338   and 7B). The number of D4-positive vesicles (per cell plane) was ~2.7 fold higher in $Npc1^{-/-}$ cells (p

339   < 0.01, n = 15) compared with wild-type fibroblasts (n = 15; Figure 7C), and the cumulative

340   fluorescence intensity of D4-positive vesicles was ~2.6-fold higher in $Npc1^{-/-}$ ($p < 0.001$) than in

341   wild-type fibroblasts (Figure 7D). These data indicate that fibroblasts lacking functional Npc1

342   accumulate cholesterol in vesicles, presumably in late endosome/lysosomes (Mukherjee and

343   Maxfield, 2004), consistent with a previous study (Higgins et al., 1999).

344   High-resolution C_m measurements revealed that G_p, normalized to vesicle capacitance (G_p/C_v),

345   decreased from 98 ± 5 pS/fF in controls (n = 172) to 83 ± 5 pS/fF in $Npc1^{-/-}$ fibroblasts (n = 121, $p <$

346   0.05, Figure 7F), indicating that increased vesicle cholesterol in $Npc1^{-/-}$ fibroblasts narrows the fusion

347   pore.

14

DISCUSSION

349 Several stages of exocytosis were proposed (Rand and Parsegian, 1986) beginning with the apposition

350 of membranes destined to fuse, which is then ending by (1) destabilization of the membranes in

351 contact, (2) coalescence of the two membrane surfaces and (3) re-stabilization of the fused

352 membranes. These end stages were considered to occur within microseconds to maintain the cell's

353 integrity. Hence, this view prompted the idea that once the fusion pore is formed, the fusion pore must

354 widen abruptly (full-fusion exocytosis). However, more recent experimental evidence revealed that

355 the fusion pore, once established, enters a stable, dynamically regulated state, with diameters ranging

356 between sub-nanometers and several hundred nanometers (Shin et al., 2018; Vardjan et al., 2007).

357 These pores can then undergo either reversible constriction or closure to limit vesicle discharge or full

358 widening (full-fusion exocytosis) to boost vesicle discharge (Kreft et al., 2018). It is generally

359 acknowledged that these transitions are regulated by proteins (Shin et al., 2018), which may also form

360 the fusion pore walls (Almers and Tse, 1990; Chang et al., 2017). Although the fusion pore was also

361 modeled to be exclusively lined by lipids (Nanavati et al., 1992), it is more likely to be a mixture of

362 proteolipids (Gasman and Vitale, 2017; Sharma and Lindau, 2018). There has been interest in how

363 cholesterol initiates and regulates the stages of regulated exocytosis (Churchward et al., 2005a;

364 Cookson et al., 2013; Mahadeo et al., 2015; Najafinobar et al., 2016; Rituper et al., 2012;

365 Rogasevskaia and Coorssen, 2006; Stratton et al., 2016; Wang et al., 2010; Xu et al., 2017); however,

366 direct evidence that membrane lipids define the dynamics of single fusion pore stages is missing. Our

367 results establish the role of a cholesterol-dependent radial force that constricts the fusion pore (Figures

368 5 and 6). This lipid-based mechanism of fusion pore regulation provides the missing evidence proving

369 that the fusion pore itself functions as a proteolipidic entity.

370 Four lines of evidence support this conclusion. First, the spontaneous negative curvature of

371 cholesterol, a structural stress factor (Rand and Parsegian, 1986), likely promotes the first step of the

372 membrane merger (Churchward and Coorssen, 2009). However, cholesterol may also play a role

373 during post-fusion stages. Upon stimulating regulated exocytosis, the fusion pore is formed, through

374 which vesicle cholesterol exits and subsequently mixes with the outer leaflet of the PM, contributing

15

375   to an asymmetric composition of the PM. Cholesterol has been shown to be unevenly distributed in

376   various cellular membranes (Ikonen, 2018). In some cell types, cholesterol accumulates in lysosomes,

377   especially in diseased states (Liscum, 2000; Mukherjee and Maxfield, 2004), and in the vesicle

378   membranes of secretory cells (Bogan et al., 2012; Mahadeo et al., 2015). Consistent with these

379   previous studies, we found that PRL-storing vesicles are rich in cholesterol (Figure 1). PRL is

380   discharged from vesicles through regulated exocytosis (Akerman et al., 1991; Stenovec et al., 2004),

381   and it appears that vesicle cholesterol is transferred to the PM along with the hormone. Stimulation of

382   regulated exocytosis reduced the density and size of the mCherry-D4-PFO (D4) labeled cholesterol-

383   rich PM domains (Figure 2). This likely reflects the delivery of vesicle cholesterol together with the

384   hormone discharge, as the surface PM deposits of fluorescently labeled hormone from vesicles

385   correlated with increased outer leaflet PM cholesterol domains (Figure 3). Both hormones and

386   cholesterol exit vesicles along a gradient; hormones are released into the extracellular space and

387   cholesterol into the PM. Furthermore, cholesterol exiting the vesicle through the fusion pore may also

388   regulate it, as tested in subsequent experiments.

389   The second line of evidence is that cholesterol depletion widens the fusion pore independently of

390    $[Ca^{2+}]_i$. Exposing cells to MβCD while monitoring amperometric discharge of vesicle cargo (Cookson

391   et al., 2013; Wang et al., 2010) revealed that cholesterol enrichment increased the persistence of the

392   pre-foot spike of the amperometric signal, which is considered to indirectly represent the leakage of

393   vesicle cargo through a narrow fusion pore before the pore dilates for full exocytotic release (Chow et

394   al., 1992). We monitored vesicle discharge in electrically excitable pituitary lactotrophs and in

395   electrically non-excitable astrocytes. Vesicle cargo, labeled by immunofluorescence in lactotrophs or

396   by the expression of fluorescently tagged peptide in astrocytes, was secreted with MβCD treatment

397   (Figure 4). Direct monitoring of fusion pore conductance, a measure of fusion pore diameter, revealed

398   that cholesterol depletion widens and cholesterol enrichment narrows the fusion pore in both cell

399   types (Figure 6).

400   Perturbations of membrane cholesterol may affect the activation of several types of Ca^{2+} channels,

401   including voltage-gated Ca^{2+} channels, thus affecting $[Ca^{2+}]_i$ (Levitan et al., 2010). Therefore, MβCD

16

402   may stimulate regulated exocytosis indirectly (Wang et al., 2010) through an increase in $[Ca^{2+}]_i$. In

403   contrast, whereas an MβCD-dependent increase in $[Ca^{2+}]_i$ was recorded in lactotrophs, a prominent

404   reduction was recorded in astrocytes (Figure S3), indicating that MβCD-dependent cholesterol

405   depletion in astrocytes widens the fusion pore in the absence of an increase in $[Ca^{2+}]_i$, and that fusion

406   pore widening is due to direct, cholesterol-driven regulation of the fusion pore.

407   Third, the molecular shape and physicochemical properties of cholesterol determine membrane

408   processes through effects on membrane curvature, including the initial membrane merger step of

409   regulated exocytosis (Churchward et al., 2008b; Jorgacevski et al., 2010; Rand and Parsegian, 1986).

410   Arguably, membrane lipids segregate to different parts of cellular membranes based on their intrinsic

411   curvature (Mukherjee et al., 1999) in addition to other mechanisms of lipid segregation (Tian and

412   Baumgart, 2009). Cholesterol distributes unevenly in cellular compartments (Ikonen, 2018; Wustner

413   and Solanko, 2015). The walls of the open fusion pore represent a highly curved structure in contact

414   with the PM. This orifice represents a boundary across which the cholesterol gradient between the

415   vesicle and the PM exerts tension. Due to this tension, a radial force is generated, which prevents

416   fusion pore widening (Figure 5C). An analogy for this are the capillary forces at the boundary of a

417   water-filled glass, which increase the water level at the glass surface. The radial force at the orifice of

418   the fusion pore is assumed to depend on the difference in cholesterol concentration between the

419   vesicle and the PM, driving the redistribution of vesicle cholesterol into the outer leaflet of the PM

420   (Figure 2). Based on this, a theoretical model of how cholesterol controls the fusion pore diameter

421   was developed (Supplemental Information). This model takes into account that the vesicle diameter

422   determines the fusion pore radius, as confirmed experimentally (Flasker et al., 2013; Jorgacevski et

423   al., 2010; Shin et al., 2018). Our model has multiple solutions for a stable fusion pore radius, in which

424   the relative interaction is proportional to the interaction energy per surface area (Supplemental

425   Information), and is, depending on the highly curved membranes at the fusion pore (Figure 5B),

426   plotted as a function of the normalized fusion pore radius (marked by arrows in Figure S6A). This

427   makes this model suitable for describing not only very narrow fusion pores (Vardjan et al., 2007), but

428   also those with much larger diameters (Shin et al., 2018). The radial force defined in this model

17

429 depends linearly on the local cholesterol availability (eq. 6; see also the direction of the forces

430 depicted in Figure 5C). We estimated the force at the fusion pore (γ_{pore}) from the dimensionless

431 transfer shear force (Γ_{pore}) in the radial direction: $\Gamma_{pore} = R_0\gamma_{pore}/8\pi k_c$, where R_0 is the vesicle

432 radius and k_c is the bending modulus (Supplemental Information). For a typical value of $\Gamma_{pore} = 0.4$

433 (Figure S6B), using $R_0 = 100$ nm and $k_c = 20k_BT$ (Rawicz et al., 2000), the estimate for γ_{pore} is 80

434 pN, essentially the same as the value reported recently for the fusion pore in chromaffin cells (Shin et

435 al., 2020). A similar range of forces affecting the fusion pore can be predicted by considering the

436 interactions between SNARE proteins at post-fusion stages of exocytosis (Jorgacevski et al., 2011).

437 The validity of this model is corroborated by the series of experiments (Figures 6I and 6J), in which

438 normalized fusion pore conductance (G_p/C_v) is correlated with cholesterol content, indicating that

439 changes in cellular cholesterol content may regulate the vesicle fusion pore in health and disease.

440 Fourth, our results provide evidence supporting the role of cholesterol redistribution between the

441 vesicle and PM in the regulation of the exocytotic fusion pore, as disease-related increases in vesicle

442 cholesterol affected the fusion pore (Figure 7F) in a manner consistent with predictions by the model

443 (Figure 5D). In Niemann-Pick disease type C1 mutations in NPC1, a protein involved in lysosome:

444 ER contact site formation and therefore indirectly facilitating sterol transport (Hoglinger et al., 2019;

445 Winkler et al., 2019), lead to an accumulation of vesicle cholesterol (Liscum, 2000; Mukherjee and

446 Maxfield, 2004). In $Npc1^{-/-}$ fibroblasts vesicles contained on average ~2-fold more cholesterol

447 (Figure 7A-D). High-resolution membrane capacitance measurements of fusion pore conductance,

448 normalized to vesicle capacitance (G_p/C_v), revealed fusion pore constriction by over 15% in these

449 fibroblasts (Figure 7). These data demonstrate that the disease-related increase in vesicle cholesterol

450 in Npc1−/− fibroblasts narrows the fusion pore, which arguably hinders the capacity of vesicle cargo

451 release. The contribution this makes to the pathophysiology of NPC therefore merits further

452 investigation.

453 Moreover, it is possible that pharmacologically induced changes in the PM cholesterol levels may also

454 affect the fusion pore and therefore indirectly affect cell function(s). Recently, it has been

18

455 demonstrated that ketamine alters the density of cholesterol in the PM (Lasic et al., 2019). This

456 anesthetic and psychotomimetic has gained much attention due to its rapid and long-lasting

457 antidepressant effects (Berman et al., 2000). Ketamine was previously considered a non-competitive

458 N-methyl-D-aspartate receptor antagonist (Sanacora et al., 2012), with an antidepressant action

459 owing to increased synthesis of brain-derived neurotrophic factor (BDNF) (Li et al., 2010), However

460 ketamine has now also been shown to inhibit the release of BDNF from astrocytes, likely by reducing

461 $[Ca^{2+}]_i$ (Stenovec et al., 2016) and stabilizing the fusion pore in a narrow flickering configuration

462 (Lasic et al., 2016). These effects are very likely due to the relatively rapid, ketamine-invoked

463 changes in cholesterol density in the PM (Lasic et al., 2019), indicating that drug-induced changes in

464 PM cholesterol may shape the signaling capacity of cells through regulation of the fusion pore

465 In summary, this paper demonstrates that stimulation of exocytosis leads to the transfer and

466 subsequent mixing of vesicle cholesterol with the outer leaflet of the PM. Cholesterol redistribution

467 through the fusion pore instigates constriction of the fusion pore through a radial force, depending on

468 the difference in cholesterol concentrations between the vesicle and the PM. This theory provides a

469 new foundation for understanding this ubiquitous membrane intermediate of eukaryotic cells, not only

470 in exocytosis but also in endocytosis, intracellular trafficking, fertilization, and viral membrane

471 penetration, for which membrane pore dynamics is a key process that is now clearly shown to involve

472 both membrane proteins and lipids.

ACKNOWLEDGMENTS

AUTHOR CONTRIBUTIONS

B.R., A.G., M.L., U.G., S.T.B., E.L., M.B. and M.S. carried out electrophysiology and imaging experiments and performed data analysis. P.S.A. and J.R.C. carried out the lipidomic analysis after cholesterol depletion in cells. A.Š. and G.A. developed and prepared the D4 cholesterol fluorescent marker. F.M.P. provided the *Npc1* deficient and control fibroblasts. B.B. developed the cholesterol-mediated radial force membrane fusion pore constriction model. R.Z., J.R.C., B.B., J.J., A.V., M.K., and M.S. discussed the design of the experiments. R.Z. directed and wrote the manuscript with help from all authors.

DECLARATION OF INTERESTS

The authors declare no competing interests.

FIGURE LEGENDS
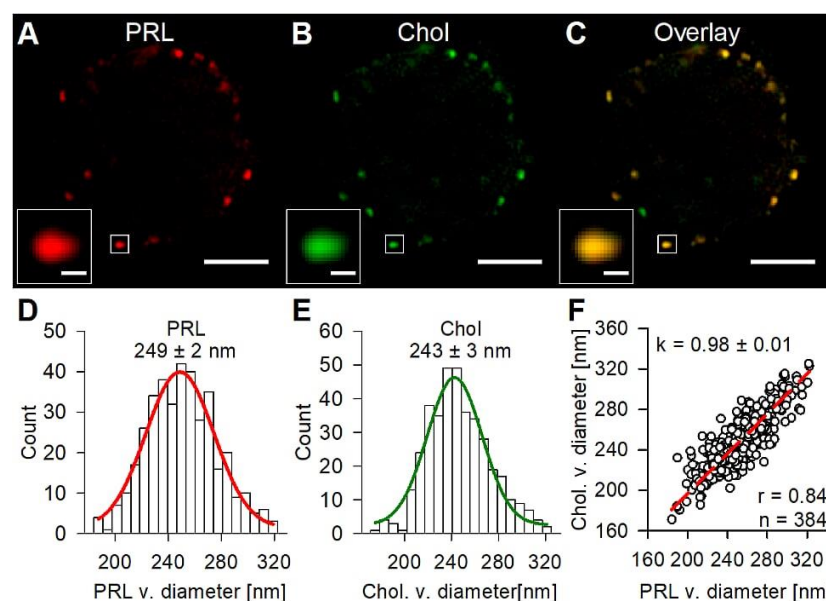
Figure 1. Secretory Vesicles Contain Prolactin (PRL) and Cholesterol (Chol)

(A–C) Deconvoluted images of a lactotroph, stained by an anti-PRL antibody (red, A) and fluorescent TopFluor-labeled cholesterol (green, B). (C) PRL and Chol signals are overlaid (colocalized pixels in yellow). Insets in the lower left corners (A–C) represent colocalized PRL and Chol in a vesicle.

20

498   (D) Frequency distribution (count) of PRL vesicles versus their diameter (PRL v. diameter).

499   The red line represents the fitted Gaussian (see also Figure S1) with a mean PRL vesicle

500   diameter of 249 ± 2 nm (n = 384; bin width, 10 nm; ten cells).

501   (E) Frequency distribution (count) of Chol vesicles versus their diameter. The green line

502   depicts the fitted Gaussian with a mean vesicle diameter of 243 ± 3 nm (n = 384; bin width,

503   10 nm; ten cells).

504   (F) PRL vesicle (v.) diameter plotted versus Chol vesicle (v.) diameter. The red line depicts a

505   linear regression (passing through the origin) of the form: Chol. v. diameter = k × PRL v.

506   diameter; correlation coefficient, r = 0.84 ($p < 0.001$); the slope of the line $k = 0.98 \pm 0.01$ (in

507   red; $p < 0.001$).

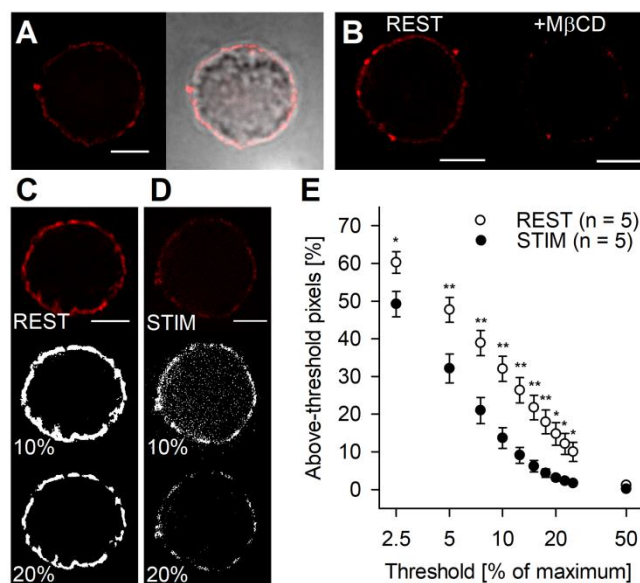508   Scale bar, 3 µm; inset scale bar, 200 nm in (A)–(C).

510   Figure 2. Stimulation of Regulated Exocytosis Decreases the Density of Cholesterol-Rich Domains in

511   the Outer Leaflet of the Plasmalemma, Labeled by mCherry-D4-PFO (D4) in Lactotrophs

512   (A) Super-resolution (left) and transmission (right) images of a D4-labeled lactotroph

513   (protocol A; Table S2), revealing the density of cholesterol-rich membrane domains in the

514   outer leaflet of the PM.

515   (B) D4-labeled lactotroph at rest (REST, left) and after cholesterol extraction with methyl-β-

516   cyclodextrin (+MβCD, 10 mM, 30 min, right).

517   (C and D) Representative structured illumination microscopy images of (C) D4-labeled

518   resting (REST, labeling protocol A) and (D) stimulated lactotrophs (STIM; 50 mM KCl,

519   labeling protocol B) and thresholded mask images (at 10% and 20% threshold, in white. See

520   STAR Methods, Figure S1, and Table S2.

521   (E) The above-threshold membrane D4-positive pixels (expressed as a percentage of all pixels

522   in the region of interest) versus the threshold (percentage of maximum) in resting (white

523   circles) and stimulated (black circles) cells. Asterisks denote a significant reduction in D4-

524   positive above-threshold pixels in the plasma membrane of stimulated (STIM) versus resting

525   (REST) lactotrophs (n > 30 optical slices from five cells per group).

526   Data are presented as means ± SEM in (E). **p < 0.01, *p < 0.05. Student's t-test in (E).

527   Scale bars, 3 μm in (A)–(D).

528

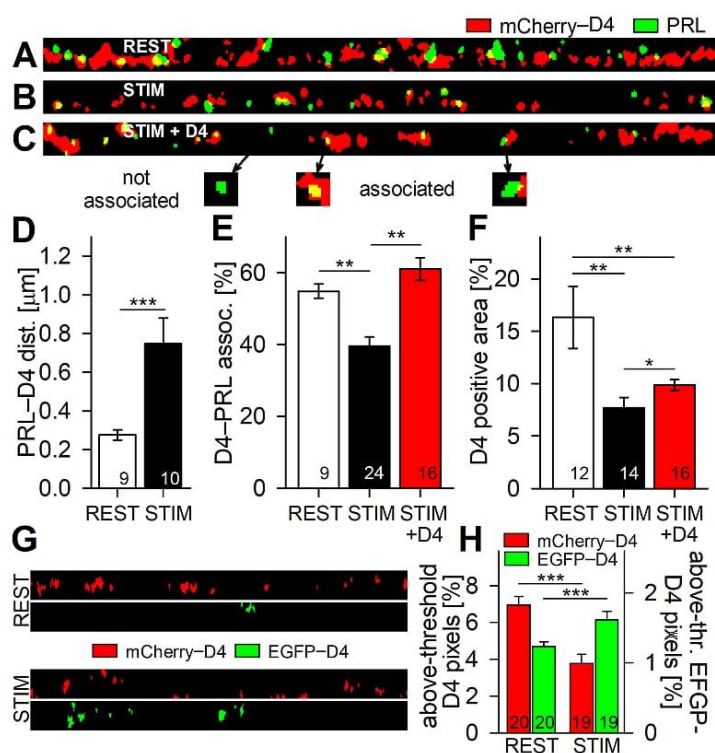529   Figure 3. Vesicle Cholesterol Delivery to the Plasmalemma (PM) is Concomitant with Vesicle

530   Prolactin (PRL) Release during Stimulated Exocytosis

531   (A) Straightened thresholded structured illumination microscopy image of the PM cell region

532   in a resting lactotroph (REST, labeling protocol C). Red, mCherry-D4 (D4); green, PRL

533   vesicles; yellow, colocalized D4- and PRL-positive pixels. See STAR Methods, Figure S1,

534   and Table S2. Note the colocalization between D4 and PRL signals, indicating association of

535   cholesterol-rich domains (D4) with released PRL vesicle cargo.

536   (B) Straightened thresholded structured illumination microscopy image of the PM cell region

537   in a stimulated lactotroph (STIM; 50 mM KCl, labeling protocol D). Red, D4; green, PRL

538   surface-attached PRL granules. Note the reduced colocalization between D4 and PRL signals,

539   indicating reduced association of cholesterol-rich domains (D4) with PRL cargo deposited on

540   the cell surface after regulated exocytosis.

541   (C) Straightened thresholded structured illumination microscopy image of the PM cell region

542   in a stimulated lactotroph (STIM + D4; with 50 mM KCl, labeling protocol E), in which D4-

543   labeling solution was also present during PRL labeling (see Table S2). Insets present

544   examples of associated D4 and PRL structures, defined as either overlaid or in contact. Note

545   that this experiment is similar to that in (B), exept that when stimulation was administered,

546   the D4 marker was present, indicating an increased association of cholesterol-rich domains

547   (D4) with PRL cargo deposited on the surface of cells after regulated exocytosis.

548   (D) The shortest distance between the D4 domain and the nearest PRL-positive structure

549   (PRL–D4 dist., in μm) in resting (REST) and stimulated (STIM) cells.

550   (E) D4 to PRL association (D4–PRL assoc., presented as the percentage of associated D4

551   structures versus all D4 structures). Note that stimulation of regulated exocytosis (STIM)

552   reduces the association of D4 domains with vesicle cargo PRL, likely due to the incorporation

553   of vesicle cholesterol into the PM.

554   (F) Relative D4-labeled membrane area (percentage of above-threshold pixels relative to all

555   pixels in the PM region) in resting (REST) and stimulated (STIM and STIM + D4) cells.

556   (G) Upper panel: Representative straightened thresholded image of the PM region of a resting

557   lactotroph (REST), labeled with D4 (upper band) followed by labeling with EGFP-D4-PFO

558   (EGFP-D4, lower band). Lower panel: Representative straightened thresholded image of the

559   PM region of a D4-labeled lactotroph (upper band) followed by labeling with EGFP-D4 after

23

560   stimulation (STIM) of regulated exocytosis with 50 mM KCl. Note that stimulation of

561   regulated exocytosis increased the EGFP-D4 labeling, whereas D4 labeling was decreased,

562   consistent with the formation of additional cholesterol-rich domains in the outer leaflet of the

563   PM via regulated exocytosis.

564   (H) The relative ratio (percentage of above-threshold pixels, relative to all pixels in the

565   thresholded image band) of D4 (red bars) and EGFP-D4 (green bars) signals in resting

566   (REST) and stimulated (STIM) cells. Note the significant decrease in mCherry-D4-positive

567   area and the significant increase in EGFP-D4 area after stimulation of regulated exocytosis,

568   indicating that new cholesterol-rich domains are formed in the PM during the exocytotic

569   fusion of vesicals with the PM.

570   The numbers in the columns indicate the number of cells analyzed. Data are represented as

571   means ± SEM. ***$p < 0.001$, **$p < 0.01$, *$p < 0.05$. Student's t-test in (D) and (H); ANOVA

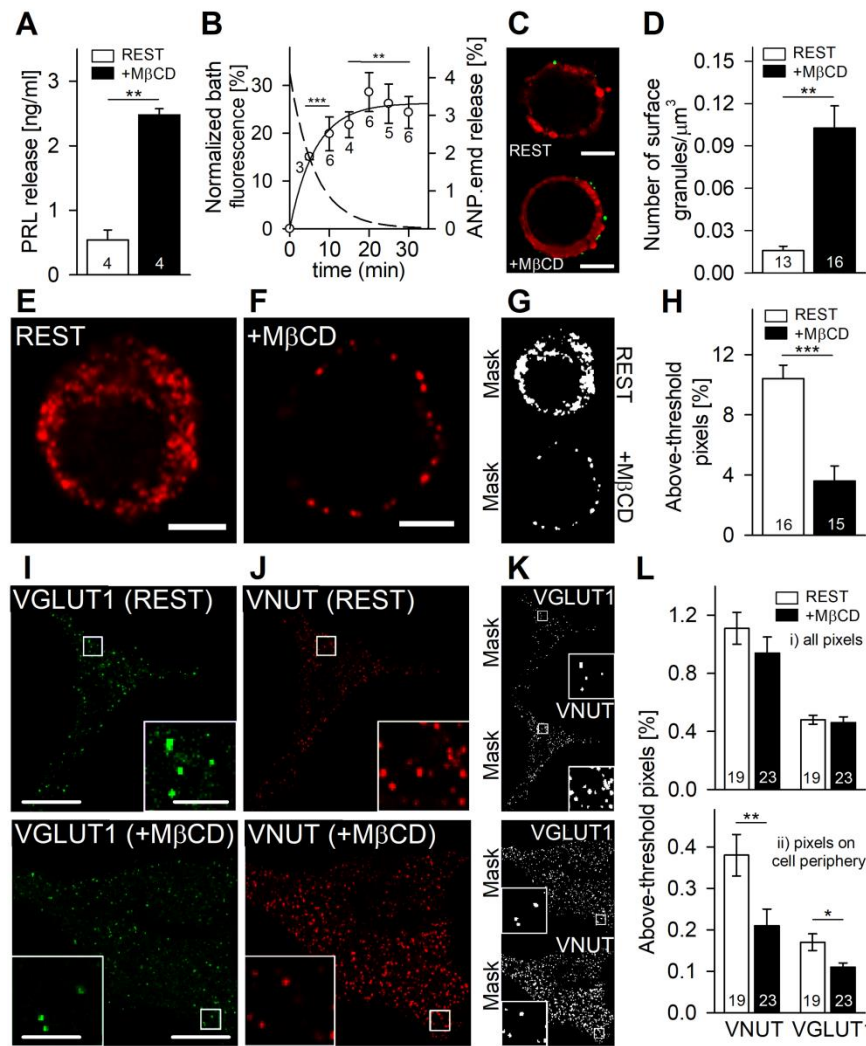572   with Holm-Sidak post-hoc test in (E) and (F).

Figure 4. Acute Cholesterol Extraction with Methyl-β-cyclodextrin (MβCD) Stimulates Vesicle Cargo Release

(A) Cumulative release of prolactin (PRL) over 30 min from resting lactotrophs and those treated with 10 mM MβCD, measured with ELISA (the numbers in the columns represent the number of parallel experiments).

(B) Normalized time-dependent increase in cell bath atrial natriuretic peptide (ANP.emd) fluorescence (%), relative to baseline (bath solution background); exponential fit (y = 26.31 × (1 − exp(−0.156t)), full line, t (time in min); and inverse function, y = 26.31 exp(−0.156t), dashed line, t (time in min) indicating time-dependent release of ANP.emd from MβCD-treated astrocytes (the numbers adjacent to the symbols represent the number of independent experiments).

585   (C) Representative structured illumination microscopy images of resting (REST) and treated

586   (+MβCD) lactotrophs (red, Vybrant DiD, a plasmalemma (PM) marker; green, surface-

587   attached vesicle cargo-PRL granules). Note the increased surface presence of PRL granules

588   after treatment with MβCD (+MβCD), indicating increased secretory activity.

589   (D) Normalized number (to cell volume, μm^3) of surface-attached PRL granules in resting

590   (REST) and MβCD-treated (+MβCD) lactotrophs (see STAR Methods).

591   (E and F) Representative confocal images of PRL vesicles (red) in (E) resting (REST) and (B)

592   treated (+MβCD) lactotrophs.

593   (G) Thresholded mask images of cells in (E) and (F). White, above-threshold pixels. Note the

594   reduced number of PRL-positive vesicles in MβCD-treated lactotrophs (+MβCD).

595   (H) The relative ratio of above-threshold PRL-positive pixels relative to all pixels in the cell

596   region in resting (REST) and MβCD-treated (+MβCD) cells.

597   (I) Representative confocal images of anti-VGLUT1-positive, i.e. glutamatergic vesicles

598   (green), in resting (REST) and treated astrocytes (+MβCD). Insets display the enlarged

599   framed areas; the bar depicts 2 μm. Note the reduced number of vesicles after treatment with

600   MβCD.

601   (J) Representative confocal images of anti-VNUT-positive, i.e. ATP-containing vesicles (red),

602   in resting (REST) and treated astrocytes (+MβCD). Insets dsiplay the enlarged framed areas.

603   Note the reduced number of vesicles after treatment with MβCD.

604   (K) Thresholded mask images of cells in (I) and (J). White, above-threshold pixels.

605   (L) The relative ratio of above-threshold pixels (%), relative to all pixels in (i) the entire cell

606   region and in (ii) the cell region adjacent to the PM in resting (REST) and treated (+MβCD)

607   astrocytes.

608   The numbers in the columns indicate the number of cells analyzed. Data are presented as

609   means ± SEM, ***$p < 0.001$, **$p < 0.01$, *$p < 0.05$. Student's t test in (A), (C), (H), and (L);

610   one-sample Student's t-test versus 0 in (D). Scale bars, 3 μm in (B), (E) and (F); 10 μm (inset,
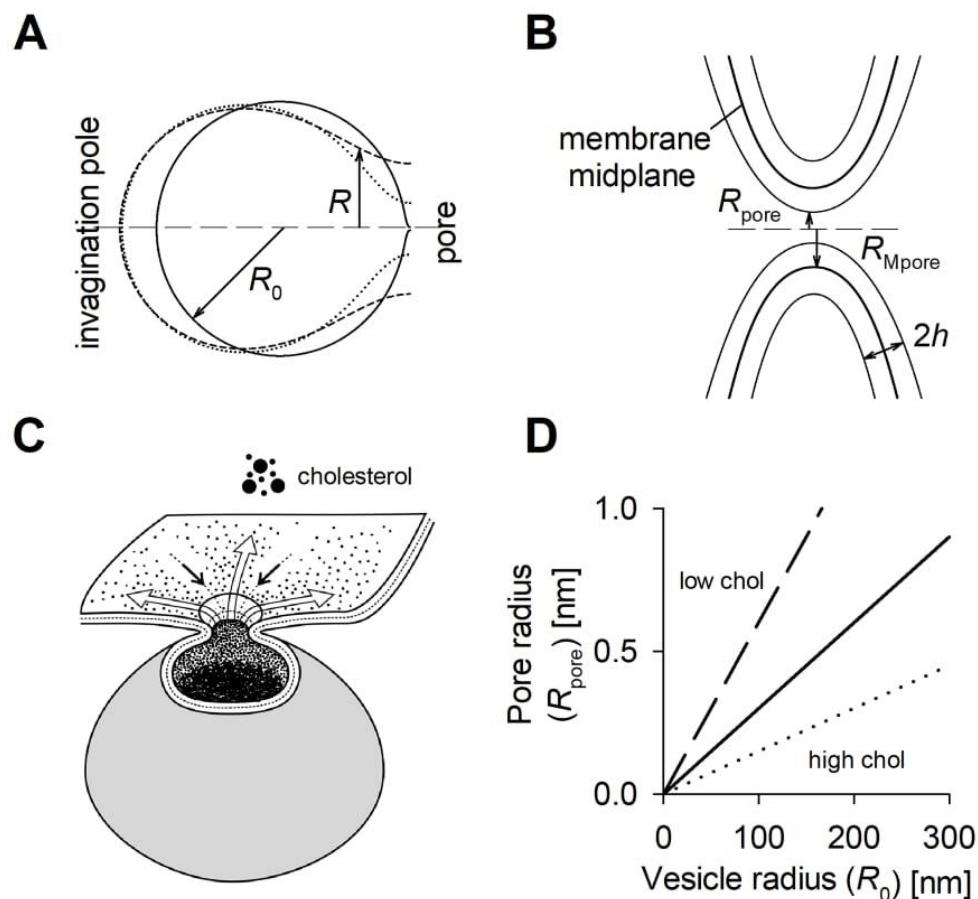
611   2 μm) in (I) and (J).

612

Figure 5. A Model of the Fusion Pore Radius as a Function of Vesicle Radius at Different Cholesterol

Concentrations between the Vesicle and Plasmalemma

(A) Longitudinal cross-sections of characteristic invagination shapes (secretory vesicle

connected by the fusion pore to the PM) at a given invagination area ($A = 4\pi R_0^2$) for $R_0 c_p =$

1.003 (full line), 1.045 (dotted line), and 1.099 (dashed line); R_0 denotes the vesicle radius, R

denotes the distance of the vesicle membrane from the symmetry axis.

(B) Scheme of the fusion pore, where R_{pore} denotes the fusion pore radius and R_{Mpore} is the

radius of the membrane midplane at the fusion pore.

(C) A scheme of the fusion pore and processes taking place when the fusion pore opens.

Vesicle cholesterol density is depicted to be very high in the vesicle membrane as well as in

the vesicle lumen, likely part of a crystalline array with hormones. Cholesterol in the

intraluminal, a negatively curved face of the vesicle membrane, exits the vesicle through the

fusion pore. However, the positive membrane curvature at the fusion pore orifice represents a

27

626 boundary/barrier for cholesterol exiting the vesicle into the outer leaflet of the PM. The white

627 arrows denote the direction of cholesterol transfer from the vesicle toward the outer leaflet of

628 the PM. This creates tension and a radial force (tips of the black arrows), keeping the fusion

629 pore radius constricted. Cholesterol molecules transferred from the vesicle membrane mix

630 with cholesterol-rich rafts in the outer-leaflet of the PM.. See Supplemental Information for

631 the development of the model.

632 (D) Dependence of the fusion pore radius (R_{pore}) as a function of the vesicle radius (R_0) for

633 the ratio $\beta/E_0 = 6 \times 10^{-3}$ (dashed line), 3×10^{-3} (full line), and 1.5×10^{-3} (dotted line)

634 (see Supplemental Information, eqs. 6 and 7, where constants $E_0, \beta,$ and α are defined) at

635 relatively large α, representing low, normal, and high cholesterol (chol.) in the PM,

636 respectively.

637

638
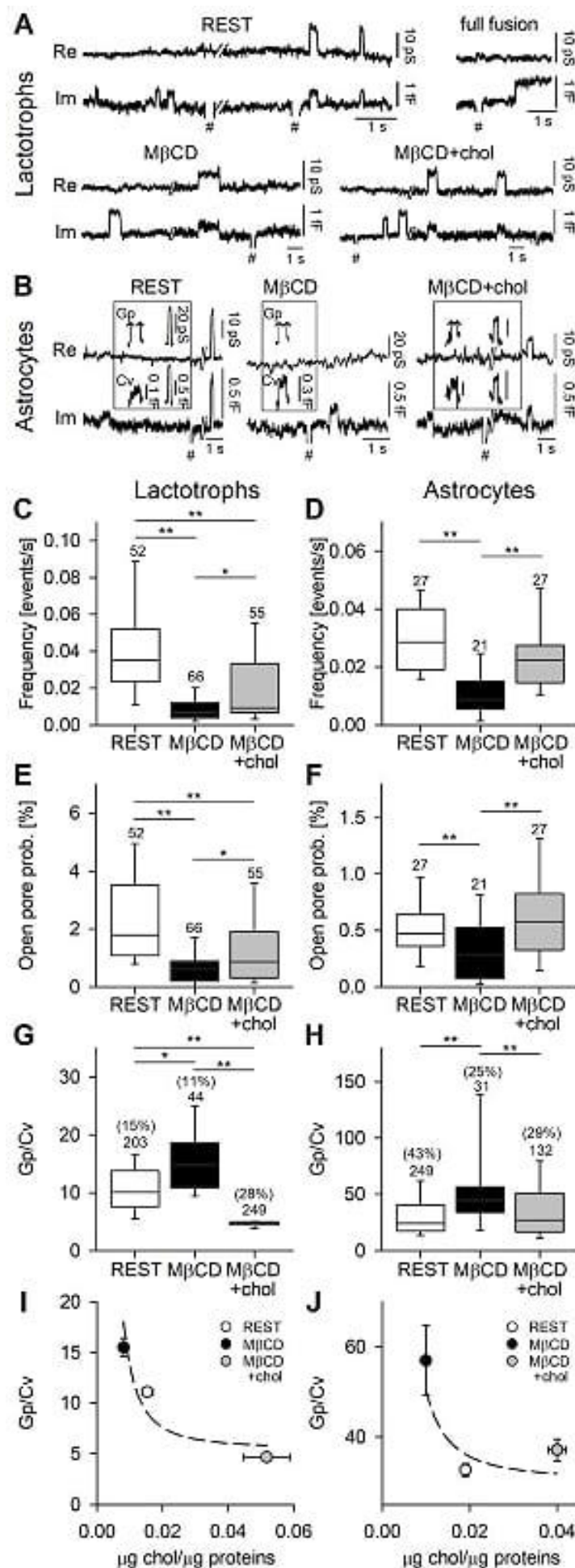
639   Figure 6. Lowering Cholesterol Decreases the Probability of Vesicle Fusion and Increases Fusion

640   Pore Conductance in Lactotrophs and Astrocytes, an Effect Rescued by Cholesterol

641   Replenishment.

642   (A) Representative patch-clamp cell-attached membrane recordings of Re (real) and Im

643   (imaginary) parts of admittance traces displaying reversible and irreversible Im discrete steps

644   (proportional to the membrane capacitance, C_m) with or without projections to Re, in resting

645   (REST), cholesterol-extracted (+MβCD), and cholesterol-replenished (MβCD + chol)

646   lactotrophs, after MβCD washout.

647   (B) Representative Re and Im traces displaying reversible discrete Im steps with or without

648   projections to Re in resting (REST), (+MβCD), and (MβCD + chol) treated astrocytes. Cells

649   in the +MβCD group in (A) and (B) were pretreated with MβCD (10 mM, 30 min) before

650   recordings. After cholesterol extraction and before recording, cholesterol was replenished

651   (MβCD + Chol) with cholesterol-replenishing solution (10 mM, 30 min).

652   (C and D) The frequency of reversible fusion events in resting (REST), (+MβCD), and

653   (MβCD + chol) lactotrophs (C) and astrocytes (D).

654   (E and F) Open (detectable) fusion pore probability in resting (REST), (+MβCD), and

655   (MβCD + chol) lactotrophs (E) and astrocytes (F).

656   (G and H) Fusion pore conductance (G_p) normalized to vesicle membrane capacitance (C_v)

657   (G_p/C_v) in resting (REST), (+MβCD), and (MβCD + chol) treated lactotrophs (G) and

658   astrocytes (H). The numbers in parentheses denote the percentage of Re projections to the Im

659   trace, relative to all transient Im events.

660   (I-J) Normalized fusion pore conductance (G_p/C_v), proportional to $(R_{pore}/R_0)^2$ (Supplemental

661   Information, eq. 7) versus normalized cholesterol concentration (μg chol/μg protein),

662   proportional to E_1 (Supplemental Information) in resting (REST), (+MβCD), and (MβCD +

663   chol) (I) lactotrophs and (J) astrocytes. Fitted (to all data pairs) inverse square curve is of the

664   form $(G_p/C_v) = (8.23 \times 10^{-4} \pm 4.35 \times 10^{-5})/x^2) + (5.33 \pm 0.23)$, r = 0.649 (I) and.

665    $(G_p/C_v) = (2.00 \times 10^{-3} \pm 5.56 \times 10^{-4})/x^2) + (30.59 \pm 1.95)$, r = 0.174 (J).

666   The numbers above the box plots indicate the number of cells analyzed in (C)–(F) and the

30

667   number of transient Im events with Re projections in (G) and (H). Data are presented as

668   medians with interquartile range (C–H) and means ± SEM in (I and J). **p < 0.01, *p < 0.05.

669   ANOVA on ranks with Dunn's post-hoc test. # denotes 10 fF calibration.
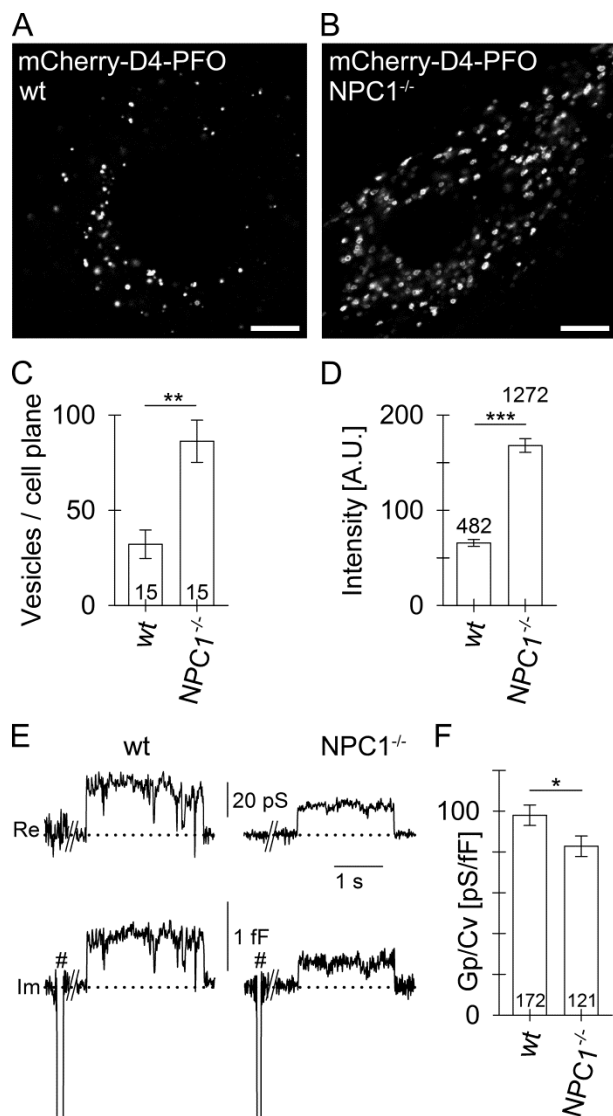
670

671

672   Figure 7. Increased Cholesterol Content in Fibroblasts Lacking Npc1 is Associated with Reduced

673   Fusion Pore Conductance

674   (A and B) Confocal images of fixed wild-type (wt) and $Npc1^{-/-}$ fibroblasts labeled with the

675   cholesterol-specific membrane-binding domain of perfringolysin O (mCherry-D4) reveal numerous

676   vesicle-like structures in the $Npc1^{-/-}$ versus wt cells (scale bar, 10 μm).

677   (C and D) Number (mean ± SEM) of mCherry-D4-positive vesicles per cell plane (C) and the

678   cumulative vesicle fluorescence intensity (D) in wt and $Npc1^{-/-}$ fibroblasts. The numbers at the

679   bottom and top of the bars indicate the number of cell images and vesicles analyzed, respectively; **p

680   < 0.01, ***p < 0.001 versus respective comparisons (Mann-Whitney U test).

681   (E) Electrophysiological recordings of real (Re, top) and imaginary (Im, bottom) parts of the

682   admittance signals in vesicles transiently interacting with the PM in wt and $Npc1^{-/-}$ fibroblasts.

683   Dotted lines indicate baseline level; # denote calibration pulses.

684   (F) Fusion pore conductance (G_p) normalized to vesicle capacitance (C_v, G_p/C_v) is reduced in $Npc1^{-/-}$

685   fibroblasts. The numbers at the bottom of the bars indicate the number of vesicles analyzed. *p < 0.05

686   (Mann-Whitney U test).
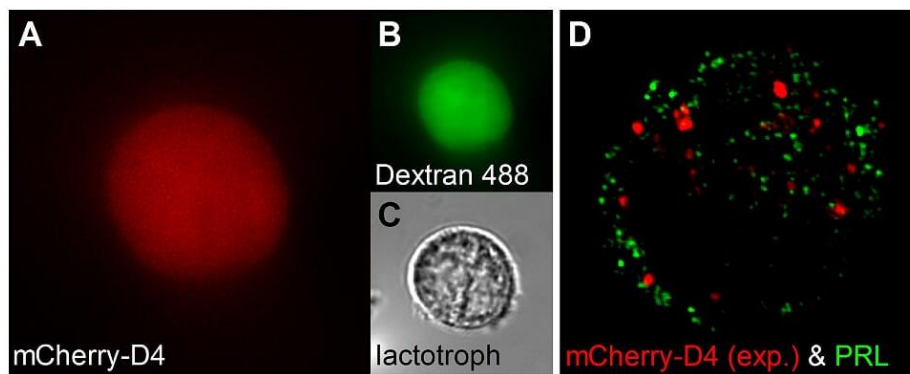
SUPPLEMENTAL FIGURES

687

688

689   Figure S1. Microinjected mCherry-D4-PFO Poorly Labels the Cytoplasmic Leaflet of the Plasmalemma
690   and the Membrane of Prolactin (PRL) Vesicles, Related to Figure 2.
691   (A–C) Representative fluorescent and transmission images of a lactotroph microinjected with
692   mCherry-D4-PFO or mCherry-D4-PFO-YQDA (red, A) alongside with Dextran Alexa 488 (green, B). (C)
693   Transmission image of the cell shown in A & B.
694   (D) Representative super-resolution microscopy image of a lactotroph. Red, expressed plasmid
695   mCherry-D4-PFO by electroporation (mCherry-D4 (exp.), see STAR Methods); green, anti-prolactin
696   antibody labeling, PRL).
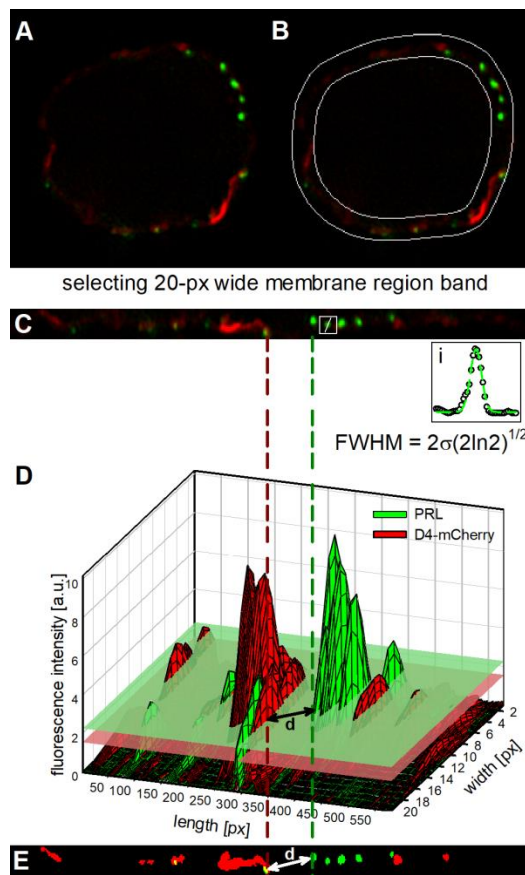697

698

699

700

Figure S2. Graphical Representation of mCherry-D4-PFO (D4) and the Prolactin (PRL) Analysis
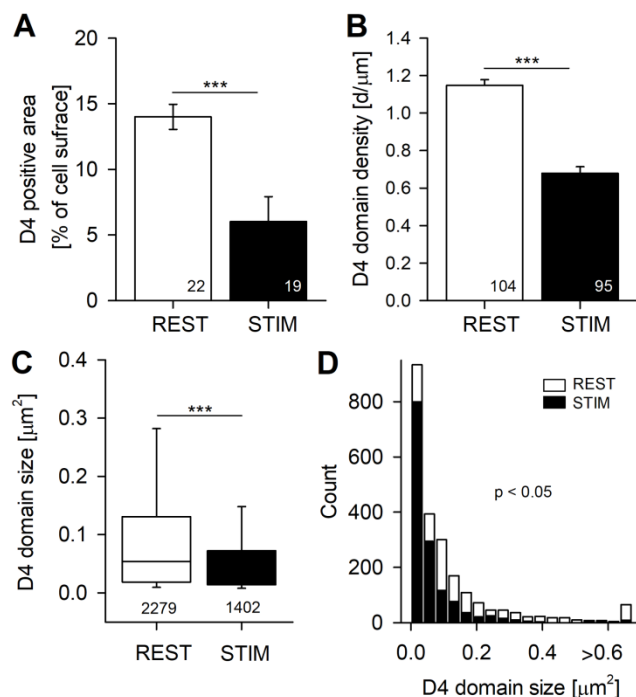
Procedure, Related to Figure 2.

(A) Representative structured illumination microscopy image of a lactotroph labeled with

mCherry-D4-PFO (red) and PRL (green).

(B) A band of the peri-plasmalemmal content of fluorescent markers. White, 20-pixel (~800

nm)-wide band encompassing the plasmalemmal region of the cell in (A).

(C) Straightened (linear) 20-pixel-wide structured illumination microscopy image of the

plasma membrane area. Inset (i): a graphical representation of the vesicle size calculation

method (vesicle diameter = FWHM = $2\sigma\sqrt{(2\ln2)}$; σ is the standard deviation of the Gaussian

fit).

(D) Graphical-3D representation of the thresholding protocol. Red D4 signal; green PRL

signal; red plane, D4 threshold; green plane, PRL threshold (see also STAR Methods). Px-

pixels for length and width.

(E) Thresholded 20-pixel-wide image of the plasma membrane region of the cell in (D). Red,

33

715   above-threshold D4 signal; green, above-threshold PRL signal. d is the shortest distance from

716   the D4 domain to the PRL-labeled structure.

717

718

719

720 Figure S3. Stimulation of Regulated Exocytosis Decreases the Density and Area of Cholesterol-Rich

721   Domains in the Outer Plasma Membrane Leaflet, Labeled by mCherry-D4-PFO (D4) in

722   Lactotrophs, Related to Figure 2.

723   We repeated the experiment shown in Figure 2E and adjusted the acquisition parameters for

724   faint signals.

725   (A) Relative D4-positive plasmalemmal (PM) area decreased significantly from $14.0\% \pm$

726   0.9% in controls (REST, n = 22) to $6.0\% \pm 1.9\%$ in exocytosis-stimulated cells (STIM, n =

727   19, $p < 0.001$).

728   (B) The density of D4-positive domains, expressed as the number of D4-positive structures

729   (d) per PM length (in µm), also significantly decreased from 1.15 ± 0.03 d/µm in controls

730   (REST, n = 104 optical slices, 12 cells) to 0.68 ± 0.04 d/µm in exocytosis-stimulated cells

34

731 (STIM, n = 95 optical slices, 13 cells, p < 0.001).

732 (C) The size of the individual D4 domains (insets in Figures 2C and 2D) was significantly

733 smaller and decreased from 0.054 μm^2 (interquartile range [IQR], 0.019–0.131, n = 2279

734 domains, 12 cells) in controls (REST) to 0.032 μm^2 (IQR, 0.014–0.072, n = 1402 domains, 13

735 cells) in exocytosis-stimulated cells (STIM, p < 0.001).

736 (D) Frequency distribution of D4 domain size in vehicle-treated (REST) and stimulated

737 (STIM; 18 bins; bin width, 0.037 μm^2) cells. Note the significant difference in distributions (p

738 < 0.05, Kolmogorov-Smirnov test).

739 The numbers in the columns indicate the number of cells analyzed in (A), the number of

740 optical slices analyzed in (B), and the number of D4 domains analyzed in (C). Data are

741 presented as means ± SEM in (A) and (B), and as median with IQR in (C), ***p < 0.001.

742 ANOVA with Holm-Sidak post-hoc test in (A), student's t-test in (B), and Mann-Whitney
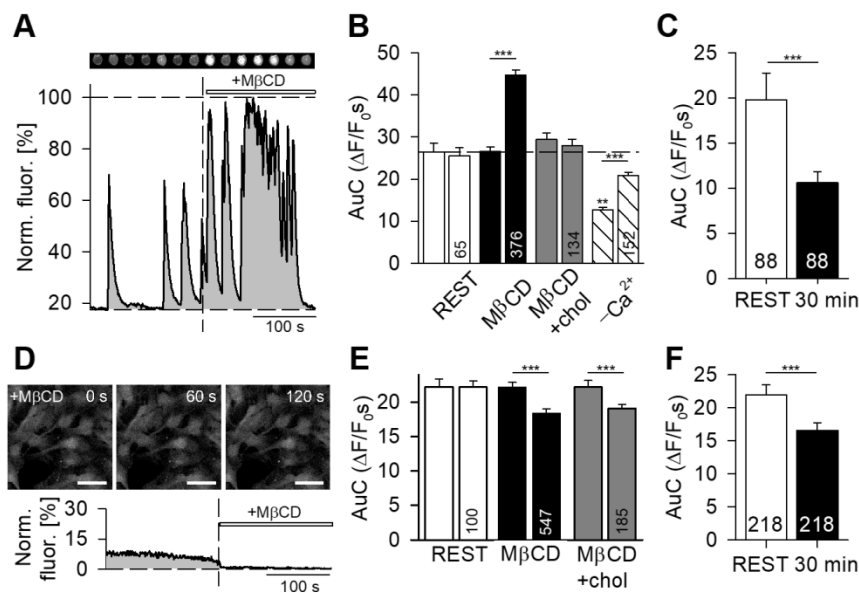
743 rank sum test in (C).

744

745 Figure S4. Cholesterol Extraction Increases Cytosolic Free Calcium Levels ($[Ca^{2+}]_i$) in Lactotrophs

746 and Decreases $[Ca^{2+}]_i$ in Astrocytes, Related to Figure 4.

747 (A) Representative confocal images of a Fluo-4-loaded ($[Ca^{2+}]_i$ marker) lactotroph (top

748 sequence) and time-dependent fluctuations in $[Ca^{2+}]_i$ (Norm. fluor. [%]) 3 min before (before

749   the vertical dashed line) and after MβCD treatment (10 mM, 3 min, after the vertical dashed

750   line).

751   (B) The area under the curve (AuC, see the gray area in A; $\Delta F/F_0 s$) 3 min before and 3 min

752   after treating lactotrophs with vehicle (REST), MβCD, cholesterol-replenishing solution

753   (MβCD + chol) and Ca^{2+}-free vehicle (-Ca^{2+}). Dashed line, resting baseline $[Ca^{2+}]_i$.

754   (C) The AuC ($\Delta F/F_0 s$) in resting (REST) and MβCD-terated (30 min) lactotrophs.

755   (D) Representative images of $[Ca^{2+}]_i$ levels in astrocytes at the time of MβCD application

756   (+MβCD, 0 s) as well as 60 s and 120 s in the presence of MβCD; and (below) the time-

757   dependent fluctuations in $[Ca^{2+}]_i$ (Norm. fluor. [%]) during resting conditions (3 min) and the

758   same cell after acute treatment with MβCD (+MβCD, 3 min). Note the reduction in $[Ca^{2+}]_i$.

759   (E) The AuC ($\Delta F/F_0 s$) 3 min before and after treatment of astrocytes with vehicle (REST) and

760   MβCD and cholesterol-replenishing solution (MβCD + chol).

761   (F) The AuC ($\Delta F/F_0 s$) in resting (REST) astrocytes and MβCD-terated (30 min) astrocytes.

762   The numbers in the bars indicate the number of cells analyzed. Data are presented as means ±

763   SEM, ***$p < 0.001$; Student's t-test. Scale bar, 20 μm in (D).
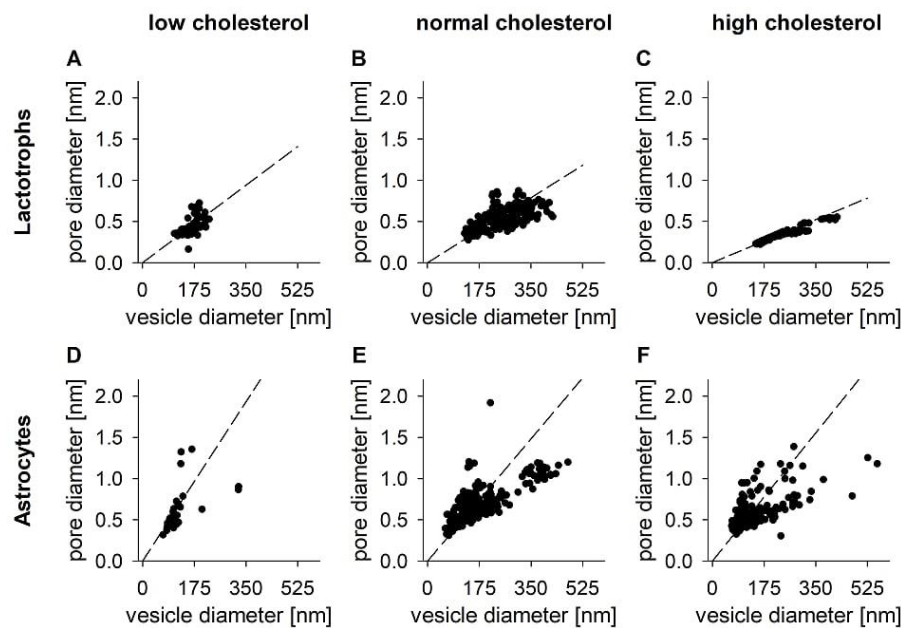
764

765

Figure S5. Theoretical Model Fitting Experiment, Related to Figure 5 and Figure 6.

The relationship between the measured values of the fusion pore diameter (estimated from the fusion pore conductance (Gp); pore diameter [nm]) and the vesicle diameter [nm], estimated from the vesicle membrane capacitance (Cv) at different cholesterol densities (low, normal and high cholesterol). The dashed lines are the best fits using eq. 9 (Supplemental Information) with values of β/E_0 denoting line slopes, which were significantly higher at low cholesterol than at normal and high cholesterol ($p < 0.05$, ANCOVA, Bonferroni corrected), both in lactotrophs and astrocytes.
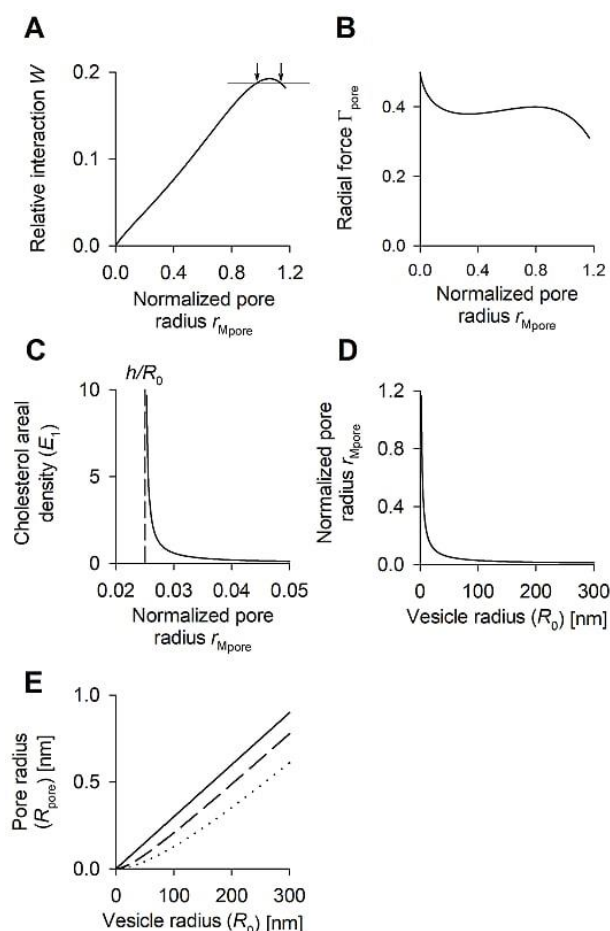
776

Figure S6. A description of the Fusion Pore Radius as a Function of the Secretory Vesicle Radius and Membrane Cholesterol Density (Concentration), Related to Figure 5.

(A) The dimensionless, relative interaction constant (W) as a function of the normalized pore radius of the membrane midplane at the fusion pore (r_{Mpore}). The arrows denote two solutions for the fusion pore radius at a given value of W (gray line).

(B) The dimensionless transfer shear force in the radial direction (radial force, Γ_{pore}) as a function of the normalized pore radius of the membrane midplane at the fusion pore (r_{Mpore}).

(C) Dependence of the cholesterol areal density in the invagination membrane (E_1), relative to the corresponding plasmalemmal density, as a function of the normalized pore radius of the membrane midplane at the fusion pore (r_{Mpore}) at $\beta = 3 \times 10^{-3} \times E_0$ and $h/R_0 = 0.025$.

(D) Dependence of the normalized pore radius of the membrane midplane at the fusion pore (r_{Mpore}) as a function of the vesicle radius (R_0) at $\alpha = 1 \text{ nm}^{-1}/E_0$, and $\beta = 3 \times 10^{-3} \times E_0$.

789   (E) Dependence of the fusion pore radius (R_{pore}) as a function of the vesicle radius (R_0) for the

790   parameter $\alpha = 1 \text{ nm}^{-1}/E_0$ (full line), $0.01 \text{ nm}^{-1}/E_0$ (dashed line), and $0.0033 \text{ nm}^{-1}/E_0$

791   (dotted line) at $\beta = 3 \times 10^{-3} \times E_0$. Lines in (A), (B), (D), and (E) end where the fusion

792   pores are completely open. See Supplemental Information for the details of the model.

793

Methods

LEAD CONTACT AND MATERIALS AVAILABILITY

Further information and requests for resources and reagents should be directed to and will be fulfilled

by the Lead Contact, Robert Zorec (robert.zorec@mf.uni-lj.si).

EXPERIMENTAL MODEL AND SUBJECT DETAILS

Materials and Solutions

Methyl-β-cyclodextrin (MβCD) and cholesterol were from Sigma-Aldrich. The cholesterol assay kit

(Amplex Red) and Vybrant DiD cell-labeling solution were from Invitrogen. All other chemicals were

of the highest purity available. The extracellular (bath) solution (ECS) for lactotrophs contained 130

mM NaCl, 5 mM KCl, 8 mM $CaCl_2$, 10 mM D-glucose, 10 mM HEPES (N-2-

hydroxyethylpiperazine-N′-2-ethanesulfonic acid) at pH 7.2 (with NaOH). The ECS for astrocytes

contained 130 mM NaCl, 5 mM KCl, 2 mM $CaCl_2$, 1 mM $MgCl_2$, 10 mM D-glucose, 10 mM HEPES

at pH 7.2 (with NaOH). In experiments with Ca^{2+}-deficient extracellular solution, $CaCl_2$ was replaced

with NaCl. The osmolarity of the ECS was ~300 mOsm.

Animals

The experiments were performed on primary lactotroph cultures isolated from 30- to 60-day-old

Wistar rats and primary astrocyte cultures isolated from 2- to 3-day-old Wistar rats. The care of the

experimental animals was in accordance with the International Guiding Principles for Biomedical

Research Involving Animals developed by the Council for International Organizations of Medical

Sciences and Directive on Conditions for Issue of License for Animal Experiments for Scientific

Research Purposes (Official Gazette of the RS, nos. 40/85 and 22/87). The research conducted was

approved by The Administration of the Republic of Slovenia for Food Safety, Veterinary and Plant

Protection (Republic of Slovenia, Ministry of Agriculture, Forestry and Food, Dunajska cesta 22,

1000 Ljubljana), document no. U34401-47/2014/7.

Cell Cultures

Lactotroph primary cultures were prepared as described (Rituper et al., 2013b). After isolation, lactotrophs were plated onto poly-L-lysine (1%, w/v)-coated coverslips and kept in high-glucose Dulbecco's modified Eagle's medium (Invitrogen) supplemented with 10% newborn calf serum and L-glutamine at 37°C with 95% humidity and 5% CO_2. Primary cortical astrocyte cultures were prepared from the cerebral cortices of neonatal rats as described (Schwartz and Wilson, 1992). Cells were grown in Dulbecco's modified Eagle's medium supplemented with 10% fetal bovine serum, 1 mM sodium pyruvate, 2 mM L-glutamine, and 5 U/mL penicillin / 5 μg/mL streptomycin at 37°C with 95 % humidity and 5% CO_2. When cells reached confluence, they were shaken overnight, trypsinized, and plated into 2-mL cell culture tubes. After reaching confluence again, they were subcultured onto 22-mm poly-L-lysine-coated (0.1 %, w/v) coverslips. Experiments were performed on lactotrophs and astrocytes within 3 days after plating.

Fibroblasts were prepared from *Npc1* null mice. Briefly, BALB/cNctr-Npc1m1N/J, (*Npc1$^{-/-}$*) and control (*Npc1$^{+/+}$*) mice were generated from heterozygous breeding. Genotyping was performed according to published methods (Loftus et al., 1997). All mice were maintained under a standard 12h light/12h dark cycle with water and food available ad libitum. All procedures were performed according to the UK Animals (Scientific Procedures) Act 1986 under a project license (PPL No. I25BD461E) from the UK Home Office. Fibroblasts were prepared from *Npc1$^{-/-}$* and *Npc1$^{+/+}$* mice according to published methods (Khan and Gasser, 2016).

METHOD DETAILS

Fluorescent (TopFluor) Cholesterol Loading

Fluorescent cholesterol (TopFluor cholesterol)-MβCD inclusion complexes were prepared as described (Rituper et al., 2013a) . Briefly, 10 mg of TopFluor cholesterol (23-(dipyrromethene boron difluoride)-24-norcholesterol) (Avanti Polar Lipids) was added to the 10 mM MβCD solution (in phosphate buffered saline [PBS], molar ratio of MβCD/cholesterol 8:1) and sonicated in an ice bath

41

843   (4°C) for 30 min protected from light. The solution was filtered through 0.2-μm filters, aliquoted, and

844   stored at −20°C until further use. To load fluorescent cholesterol into prolactin (PRL) secretory

845   vesicles, lactotroph-loaded coverslips were washed with PBS and incubated with 1 mL of loading

846   solution, diluted to a TopFluor cholesterol concentration of 50 μg/mL at 37°C and 5% CO_2 for 60

847   min. After thorough washing (in PBS), loading solution was replaced with standard lactotroph culture

848   medium for 8−10 h. High background fluorescence could be diminished by a brief (2 min) incubation

849   of cells with 10 mM MβCD solution.

Immunocytochemistry

851   PRL granules attached to the cell surface were immunolabeled by first blocking nonspecific

852   immunoreactive sites with 3% bovine serum albumin (BSA/PBS) and then tagging the PRL antigens

853   with primary mouse monoclonal anti-PRL antibodies (1:300; Thermo Scientific) for 10 min at room

854   temperature (RT). To immunolabel PRL secretory vesicles, cells were fixed and permeabilized with

855   2% formaldehyde (10 min, RT) and incubated in 3% BSA and 10% goat serum in PBS (1 h, 37°C).

856   PRL vesicles were labeled with primary mouse monoclonal anti-PRL antibodies (1:300, Thermo

857   Scientific) for 2 h at 37°C. Primary anti-PRL antibodies were localized using secondary anti-mouse

858   antibodies conjugated to specified Alexa fluorophores (1:600, 45 min, 37°C). Glutamatergic and

859   ATP-containing vesicles were immunolabeled by fixing astrocytes with 4% formaldehyde (15 min,

860   RT). Astrocytes were then incubated in 3% BSA and 10% goat serum in PBS (1 h, 37°C). Next,

861   primary mouse monoclonal anti-VGLUT1 antibodies (1:800; SySy) were added for 2 h at 37°C and

862   then primary rabbit polyclonal anti-VNUT antibodies (1:200, from Prof. Yoshinori Moriyama) for 2 h

863   at 37°C, followed by the addition of both secondary antibodies conjugated to specified Alexa

864   fluorophores (1:600, 45 min, 37°C). SlowFade Gold antifade reagent was used to mount coverslips to

865   glass slides (Invitrogen).

EGFP-D4-PFO- and mCherry-D4-PFO Expression and Purification

The perfringolysin O (PFO) D4 domain with N-terminal EGFP (EGFP-D4-PFO) or mCherry (mCherry-D4-PFO) fusion was expressed and purified as described previously (Lasic et al., 2019). Briefly, an EGFP- or mCherry-tagged D4 DNA fragment coding for the amino acids from S386 to N500 was introduced into the pET8c vector using XhoI and MluI sites. The resulting expression plasmid encoded for N-terminal 6xHis-tag followed by the recognition site for TEV protease and the EGFP/mCherry coding region separated from the D4 PFO domain with 10 amino acids long GS linker. The integrity of each plasmid was verified by DNA sequencing of its entire open reading frame. For recombinant protein production, a freshly transformed *Escherichia coli* BL21(DE3) strain was used, which was grown at 37°C in LB medium supplemented with 100 µg/mL ampicillin. Overexpression of the fluorescently tagged D4 domain was induced with 0.5 mM isopropyl β-D-1-thiogalactopyranoside (IPTG) at OD_{600} from 0.5 to 0.7 for 16−18 h at 20°C. The cells were harvested by centrifugation, resuspended in 10 mL/g wet mass of lysis buffer (50 mM NaH_2PO4, 300 mM NaCl, 10 mM imidazol [pH 8.0]) and lysed by sonication. Recombinant proteins were purified by nickel chromatography (Ni-NTA Superflow; Qiagen) using the same procedures as described previously (Lasic et al., 2019). Purified protein was dialyzed against Tris-HCl buffer (50 mM Tris-HCl, 200 mM NaCl, 5% (v/v) glycerol [pH 7.4]) using Slide-a-lyzer with a molecular weight cutoff of 10 kDa (Thermo Scientific). Purification was confirmed by SDS-PAGE and Coomassie staining.

D4-PFO Membrane and Organelle Labeling, and D4-PFO Expression in Mammalian Cells

To label the exoplasmic leaflet of lactotroph PM, cells were first rinsed with PBS followed by incubation with 1 µM mCherry-D4-PFO or EGFP-D4-PFO in 3% BSA for 30 min at RT. After washing, cells were fixed with 2% formaldehyde. In some experiments, cells were further immunolabeled as described in the Results (Figure 3). In addition to the labeling, the mCherry-D4-PFO-encoding plasmid was also expressed in lactotrophs. For this purpose, gene fragment coding for

43

891 mCherry-D4 fusion from the bacterial expression plasmid described above was amplified with the

892 following pair of primers: 5′-CGT ACA AGC TTA TGC ATC ACC ATC ACC ATC AC-3′ (sense)

893 and 5′-GCA TGT GGA TCC AGT ACG CGT TTA ATT GTA AGT AAT ACT-3′ (antisense). The

894 PCR product was cloned into the pcDNA3 vector using HindIII and BamHI restriction sites. The

895 sequence of the constructed plasmid was confirmed by DNA sequencing. Electroporation was used to

896 transfect plasmids into lactotrophs using a Basic Nucleofector Kit for Primary Mammalian Epithelial

897 Cells (Lonza, program W-001) (Figure S1).

898 To examine the distribution of cholesterol-rich membranous organelles in fibroblasts (wild-type and

899 NPC1$^{-/-}$ lacking the vesicle cholesterol transporter Niemann-Pick Type C1), cells were washed (3

900 min) with PBS, fixed in formaldehyde (2% in PBS) for 10 min, washed three times (3 min) with PBS,

901 exposed to D4-PFO-mCherry (0.25 μM) for 30 min, and washed three times with PBS (3 min); all at

902 RT. Finally, coverslips were mounted onto glass slides using SlowFade Gold antifade mountant

903 (Thermo Scientific).

Plasma Membrane Labeling with Vybrant DiD Solution

905 In some experiments, plasma membrane was labeled with 25 μM Vybrant DiD cell-labeling solution

906 (Invitrogen) for 10 min at RT. Cells were then fixed in 2% formaldehyde and mounted on glass slides

907 using SlowFade Gold antifade reagent (Invitrogen).

QUANTIFICATION AND STATISTICAL ANALYSIS

Electrophysiological Measurements

910 Cell-attached capacitance measurements were performed with a dual-phase lock-in patch-clamp

911 amplifier (SWAM IIC; Celica) as described (Rituper et al., 2013b). All experiments were performed

912 at RT. Individual recordings lasted 1,000 s. We used fire-polished pipettes, heavily coated with

913 Sylgard and with a tip resistance of 2–5 MΩ. The bath and pipettes contained ECS. A sine wave (111

914 mV rms and 1591 Hz for lactotrophs and 111 mV rms and 6364 Hz for astrocytes) was applied to the

915   pipette, and the pipette potential was held at 0 mV. During the experiments, the phase angle was

916   adjusted to nullify the changes in the real (Re) trace in response to the manually generated 10 fF

917   calibration pulses. Vesicle capacitance (C_v) and fusion pore conductance (G_p) were calculated from

918   the imaginary (Im) and real (Re) parts of the admittance traces as reported previously (Lollike and

919   Lindau, 1999): $C_v = [(Re^2 + Im^2)/Im]/\omega$, where ω is the angular frequency ($\omega = 2\pi f$, f is the sine wave

920   frequency) and $G_p = (Re^2 + Im^2)/Re$. The fusion pore radius was estimated using the equation $G_p =$

921    $(\pi R_{pore}^2)/(\rho\lambda)$, where R_{pore} represents the fusion pore radius, ρ is the estimated resistivity of saline (100

922   Ω cm), and λ the estimated length of a gap junction channel (15 nm) (Spruce et al., 1990). The vesicle

923   diameter was calculated using a specific membrane capacitance (C_{sm}) of 8 fF/μm^2 (lactotrophs) or 10

924   fF/μm^2 (astrocytes) as described (Rituper et al., 2013b). We used a custom-written MATLAB (Math

925   Works) subroutine (CellAn; Celica) to analyze fusion events.

Total Cell Cholesterol Measurements

927   The total cell cholesterol (with cholesterol esters) was determined using the Amplex Red Cholesterol

928   Assay Kit (Invitrogen). Cells were isolated as described above, however, no serum or serum

929   substitutes were used. Samples were treated with 10 mM MβCD for 30 min at 37°C in a 5% CO_2

930   atmosphere. For cholesterol replenishment, cells were washed and resuspended in 10 mM cholesterol

931   loading solution (MβCD/cholesterol molar ratio of 8:1), prepared as described previously

932   (Churchward et al., 2005b) for an additional 30 min. Subsequently, cells were lysed with CelLytic

933   (Sigma-Aldrich), mixed with Amplex Red reagent, and incubated for 60 min at 37°C in a 5% CO_2

934   atmosphere. The resulting fluorescence was measured using an EnSpire 2300 Multimode Plate Reader

935   (PerkinElmer) with excitation at 560 nm and fluorescence emission detected at 590 nm.

Prolactin Release Measurements

937   To measure PRL release, lactotrophs were densely plated on 22-mm coverslips and treated with

938   vehicle or 10 mM MβCD for 30 min. Then, the bath solution was collected, and the rat PRL enzyme

939   immunoassay (ELISA) was performed according to the manufacturer's instructions (A05101, SPI bio;

940   Bertin Pharma).

ANP.emd Release Measurements

942   Astrocytes were transfected with the plasmid encoding atrial natriuretic peptide tagged with emerald

943   green fluorescent protein (ANP.emd; a gift from Dr. Ed Levitan, University of Pittsburgh, Pittsburgh,

944   PA, USA) using a Rat Astrocyte Nucleofector Kit (Lonza). Transfected cells were resuspended in

945   culture medium and subcultured onto poly-L-lysine-coated coverslips or 24-well plates (Nunc,

946   Thermo Scientific) and maintained at 37°C in an atmosphere of 5% CO_2 for 48–72 h. The release of

947   ANP.emd was estimated by measuring the fluorescence intensity of the bath solution at specified time

948   points (EnSpire microplate reader; PerkinElmer) at the emission wavelength of 508 nm. Fluorescence

949   was excited at 488 nm. Background fluorescence was subtracted, and the measured values were

950   averaged and expressed as a relative increase in fluorescence, normalized to controls. A one-sample t-

951   test was used for statistical comparison.

Calcium Measurements

953   Cells were loaded with 2 µM Fluo-4 AM (Molecular Probes) for 30 min in ECS. After rinsing in ECS

954   or Ca^{2+}-free ECS for 15 min, the cells were placed into the recording chamber and imaged with a

955   confocal laser scanning microscope (Zeiss LSM 780). Measurements were performed with a Zeiss

956   Plan-Apochromat oil immersion objective (40×, NA 1.3). An Ar-ion laser was used to excite Fluo-4

957   in combination with a 505-nm long-pass emission filter. Time-lapse images were acquired at a

958   sampling rate of 1 Hz. First, baseline fluorescence intensities were recorded for 3 min (F_0). Then, cells

959   were treated with either vehicle, 10 mM MβCD, or 10 mM cholesterol loading solution, and

960   fluorescent images were acquired for an additional 3 min. To assess the effect of prolonged exposure

961   to MβCD, fluorescence images were acquired for the initial 3 min and then for an additional 3 min

962   after 30 min of incubation with MβCD. Fluo-4 fluorescence, which reports changes in $[Ca^{2+}]_i$, was

963   measured in a region of interest covering the entire cell image. Resulting time-dependent fluorescence

46

964   intensity traces were first normalized to the maximal fluorescence intensity in a given trace. The

965   fluorescence intensity change was defined as $\Delta F/F_0 = (F(t) - F_0)/F_0$, expressed as a percentage. F_0 is

966   the average non-stimulated fluorescence intensity of ten frames with the lowest relative intensity of

967   fluorescence, and $F(t)$ is the relative fluorescence intensity at a given time (Figure S4).

Lipid Extraction and HPTLC Analysis

969   Cells (astrocytes) were lysed with CelLytic M (Sigma-Aldrich) and lipids were extracted as described

970   (Churchward et al., 2005b). Lysed cells were suspended in PBS, and CH_3OH and $CHCl_3$ were added

971   sequentially at a ratio of 0.8:2:1 (PBS/CH_3OH/$CHCl_3$, v/v/v), followed by vortexing and sonication

972   for 30 s. An aqueous solution of 1 M NaCl and 0.1 M HCl was added, followed by the addition of

973    $CHCl_3$ to reach a final ratio of 1.8:2:2 (PBS/CH_3OH/$CHCl_3$, v/v/v). The sample was vortexed

974   vigorously after each addition. The lower organic phase was dried under N_2 and dissolved in

975    $CHCl_3$/CH_3OH (2:1) for automated high-performance thin-layer chromatography (HPTLC) using the

976   CAMAG AMD 2 system. Silica gel 60 plates (Merck) were pre-washed with CH_3OH/$C_4H_8O_2$ (6:4

977   v/v), and heat activated at 110°C for 30 min before analysis. Neutral lipids and phospholipids were

978   resolved as previously described (Churchward et al., 2008a), detected using copper sulfate charring,

979   and imaged using the LAS 4000 Biomolecular Imager (GE Healthcare). Images were analyzed using

980   Multi Gauge Software (FUJIFILM Corporation) or ImageJ (NIH). Fluorescence of control samples

981   was defined as 100%, and changes in lipid concentrations after treatment with MβCD are reported

982   relative to corresponding controls.

Microscopy and Image Analysis

984   Except where stated otherwise, structured illumination microscopy (Zeiss Elyra PS1) was used to

985   image fluorescently labeled cells. Images were acquired with a Zeiss Plan-neofluar oil immersion

986   objective (63×, NA 1.4). Cells were illuminated with laser lines of 488 nm and/or 561 nm, and the

987   emitted fluorescence was collected through band-pass emission filters (495–560 nm and 570–650 nm,

988   respectively). Unless specified otherwise, 200-nm-thick Z stacks were acquired with an EMCCD

989   camera (16-bit, Andor iXon 885; Andor Technology) with variable exposure and analyzed with

990   ImageJ.

991   Analysis of D4-PFO-Labeled Plasma Membrane Domains

992   D4-PFO labeling and analysis protocols are depicted schematically in Figure S1. Briefly, after

993   labeling with D4-PFO (and PRL in some experiments), single (D4-PFO) or dual channel (D4-PFO

994   and PRL) fluorescent images were acquired and a 200 nm interval Z stack image was constructed for

995   every cell. Then a 20-pixel-wide band covering the plasma membrane region was selected in every

996   image within the stack (5–15 optical slices per cell), straightened, and thresholded automatically using

997   the methods for D4-PFO (Kapur et al., 1985) and PRL labeling (Tsai, 1995). Thresholded images

998   were further analyzed as described in Figure 3.

999   Surface-Attached PRL Cargo Granules Count

1000   Structured illumination microscopy images within the Z stack of lactotrophs (labeled for surface PRL

1001   granules; see Table S2) were recorded at 200 nm intervals, and the resulting Z stacks were used to

1002   reconstruct imaged cells in 3D. The 3D Objects Counter plugin (Bolte and Cordelieres, 2006) for

1003   ImageJ was used to calculate the number of PRL surface granules. Results were normalized to the cell

1004   volume, which was calculated as described (Rituper et al., 2013a).

1005   Estimation of Secretory Vesicle Quantity

1006   Confocal laser scanning microscopy (Zeiss LSM 780) was used to image immunolabeled vesicles in

1007   fixed permeabilized lactotrophs and astrocytes. Images were acquired with a Zeiss Plan-Apochromat

1008   oil immersion objective (63×, NA 1.4). For excitation of Alexa Fluor 488, an Ar-ion laser was used in

1009   combination with a band-pass emission filter (505–530 nm), and for excitation of Alexa Fluor 543, a

1010   He-Ne laser was used in combination with a long-pass emission filter (cutoff below 560 nm). Imaged

1011   cells were Z sectioned at 400-nm-thick intervals. Fluorescence images were thresholded automatically

1012   using an iterative selection method (Ridler and Calvard, 1978) for lactotrophs and another method

1013   (Kapur et al., 1985) for astrocytes. The percentage cell area (in an optical slice) positive for

1014   immunolabeled vesicles was calculated by dividing above-threshold pixels with all the pixels in a

1015 region of interest covering the entire cell (cell borders were determined with the help of transmission

1016 images).

1017 Analysis of D4-PFO-Labeled Membranous Organelles in Fibroblasts

1018 To estimate the vesicle counts and vesicle intensity, confocal images were analyzed with ImageJ. The

1019 minimum fluorescent spot taken to identify an individual vesicle in a confocal image was three

1020 adjacent pixels (0.132 × 0.132 μm), and the minimum surface area covered by a spot was 0.052 μm^2.

1021 Considering that the minimum D4-PFO-positive vesicle consisted of three adjacent pixels, a broad

1022 span of vesicles with different sizes and intensity was covered by this analysis.

Statistical Tests

1023

1024 Experimental data were compared with either the Student's t test, one-way ANOVA with Holm-

1025 Sidak's post-hoc test or ANOVA on ranks with Dunn's post-hoc test, as indicated. Depending on the

1026 distribution, the data are presented as means ± SEM or medians with interquartile range. Differences

1027 were considered significant at *$p < 0.05$, **$p < 0.01$, and ***$p < 0.001$. Statistical analyses were

1028 carried out using SigmaPlot (Systat Sofware). Data in Figure S5 were fitted using standard model

1029 linear regression, and the slopes were statistically compared with the analysis of covariance

1030 (ANCOVA) method.

DATA AND CODE AVAILABILITY

1031

1032 The datasets supporting the current study are available from the corresponding author on request, as

1033 these have not been deposited in a public repository because of potential patent application.

SUPPLEMENTAL INFORMATION

1034

1035 Supplemental Information can be found in the attached file.

SUPPORTING CITATIONS

1036

1037 The following references appear in the Supplemental Information: (Deuling and Helfrich, 1976;

1038 Helfrich, 1973; Heuser, 1989; Julicher and Lipowsky, 1996; Julicher and Seifert, 1994; Kuchel and

1039 Ralston, 1988; Seifert et al., 1991; Svetina and Zeks, 1989).

REFERENCES

Akerman, S.N., Zorec, R., Cheek, T.R., Moreton, R.B., Berridge, M.J., and Mason, W.T. (1991). Fura-2 imaging of thyrotropin-releasing hormone and dopamine effects on calcium homeostasis of bovine lactotrophs. Endocrinology *129*, 475-488.

Almers, W., and Tse, F.W. (1990). Transmitter release from synapses: does a preassembled fusion pore initiate exocytosis? Neuron *4*, 813-818.

Alvarez de Toledo, G., Fernandez-Chacon, R., and Fernandez, J.M. (1993). Release of secretory products during transient vesicle fusion. Nature *363*, 554-558.

Baumgart, T., Hess, S.T., and Webb, W.W. (2003). Imaging coexisting fluid domains in biomembrane models coupling curvature and line tension. Nature *425*, 821-824.

Berman, R.M., Cappiello, A., Anand, A., Oren, D.A., Heninger, G.R., Charney, D.S., and Krystal, J.H. (2000). Antidepressant effects of ketamine in depressed patients. Biol Psychiatry *47*, 351-354.

Bogan, J.S., Xu, Y., and Hao, M. (2012). Cholesterol accumulation increases insulin granule size and impairs membrane trafficking. Traffic *13*, 1466-1480.

Bolte, S., and Cordelieres, F.P. (2006). A guided tour into subcellular colocalization analysis in light microscopy. Journal of Microscopy-Oxford *224*, 213-232.

Brose, N., Brunger, A., Cafiso, D., Chapman, E.R., Diao, J., Hughson, F.M., Jackson, M.B., Jahn, R., Lindau, M., Ma, C.*, et al.* (2019). Synaptic vesicle fusion: today and beyond. Nat Struct Mol Biol *26*, 663-668.

Chang, C.W., Chiang, C.W., and Jackson, M.B. (2017). Fusion pores and their control of neurotransmitter and hormone release. J Gen Physiol *149*, 301-322.

Chen, Z., and Rand, R.P. (1997). The influence of cholesterol on phospholipid membrane curvature and bending elasticity. Biophys J *73*, 267-276.

Chow, R.H., von Ruden, L., and Neher, E. (1992). Delay in vesicle fusion revealed by electrochemical monitoring of single secretory events in adrenal chromaffin cells. Nature *356*, 60-63.

Churchward, M.A., Brandman, D.M., Rogasevskaia, T., and Coorssen, J.R. (2008a). Copper (II) sulfate charring for high sensitivity on-plate fluorescent detection of lipids and sterols: quantitative analyses of the composition of functional secretory vesicles. J Chem Biol *1*, 79-87.

Churchward, M.A., and Coorssen, J.R. (2009). Cholesterol, regulated exocytosis and the physiological fusion machine. Biochem J *423*, 1-14.

Churchward, M.A., Rogasevskaia, T., Brandman, D.M., Khosravani, H., Nava, P., Atkinson, J.K., and Coorssen, J.R. (2008b). Specific lipids supply critical negative spontaneous curvature--an essential component of native Ca2+-triggered membrane fusion. Biophys J *94*, 3976-3986.

Churchward, M.A., Rogasevskaia, T., Hofgen, J., Bau, J., and Coorssen, J.R. (2005a). Cholesterol facilitates the native mechanism of Ca2+-triggered membrane fusion. J Cell Sci *118*, 4833-4848.

Churchward, M.A., Rogasevskaia, T., Hofgen, J., Bau, J., and Coorssen, J.R. (2005b). Cholesterol facilitates the native mechanism of Ca2+-triggered membrane fusion. Journal of Cell Science *118*, 4833-4848.

Cochilla, A.J., Angleson, J.K., and Betz, W.J. (1999). Monitoring secretory membrane with FM1-43 fluorescence. Annu Rev Neurosci *22*, 1-10.

Cookson, E.A., Conte, I.L., Dempster, J., Hannah, M.J., and Carter, T. (2013). Characterisation of Weibel-Palade body fusion by amperometry in endothelial cells reveals fusion pore dynamics and the effect of cholesterol on exocytosis. J Cell Sci *126*, 5490-5499.

Deuling, H.J., and Helfrich, W. (1976). Red blood cell shapes as explained on the basis of curvature elasticity. Biophys J *16*, 861-868.

Flasker, A., Jorgacevski, J., Calejo, A.I., Kreft, M., and Zorec, R. (2013). Vesicle size determines unitary exocytic properties and their sensitivity to sphingosine. Mol Cell Endocrinol *376*, 136-147.

1093 Gasman, S., and Vitale, N. (2017). Lipid remodelling in neuroendocrine secretion. Biol Cell
1094 *109*, 381-390.

1095 Grabner, C.P., and Moser, T. (2018). Individual synaptic vesicles mediate stimulated
1096 exocytosis from cochlear inner hair cells. Proc Natl Acad Sci U S A *115*, 12811-12816.

1097 Gucek, A., Jorgacevski, J., Singh, P., Geisler, C., Lisjak, M., Vardjan, N., Kreft, M., Egner,
1098 A., and Zorec, R. (2016). Dominant negative SNARE peptides stabilize the fusion pore in a
1099 narrow, release-unproductive state. Cell Mol Life Sci *73*, 3719-3731.

1100 Gundersen, V., Storm-Mathisen, J., and Bergersen, L.H. (2015). Neuroglial Transmission.
1101 Physiol Rev *95*, 695-726.

1102 He, L., Wu, X.S., Mohan, R., and Wu, L.G. (2006). Two modes of fusion pore opening
1103 revealed by cell-attached recordings at a synapse. Nature *444*, 102-105.

1104 Helfrich, W. (1973). Elastic properties of lipid bilayers: theory and possible experiments. Z
1105 Naturforsch C *28*, 693-703.

1106 Heuser, J.E. (1989). Review of electron microscopic evidence favouring vesicle exocytosis
1107 as the structural basis for quantal release during synaptic transmission. Q J Exp Physiol *74*,
1108 1051-1069.

1109 Higgins, M.E., Davies, J.P., Chen, F.W., and Ioannou, Y.A. (1999). Niemann-Pick C1 is a
1110 late endosome-resident protein that transiently associates with lysosomes and the trans-
1111 Golgi network. Mol Genet Metab *68*, 1-13.

1112 Hoglinger, D., Burgoyne, T., Sanchez-Heras, E., Hartwig, P., Colaco, A., Newton, J., Futter,
1113 C.E., Spiegel, S., Platt, F.M., and Eden, E.R. (2019). NPC1 regulates ER contacts with
1114 endocytic organelles to mediate cholesterol egress. Nat Commun *10*, 4276.

1115 Holtta-Vuori, M., Uronen, R.L., Repakova, J., Salonen, E., Vattulainen, I., Panula, P., Li, Z.,
1116 Bittman, R., and Ikonen, E. (2008). BODIPY-cholesterol: a new tool to visualize sterol
1117 trafficking in living cells and organisms. Traffic *9*, 1839-1849.

1118 Ikonen, E. (2018). Mechanisms of cellular cholesterol compartmentalization: recent insights.
1119 Curr Opin Cell Biol *53*, 77-83.

1120 Jorgacevski, J., Fosnaric, M., Vardjan, N., Stenovec, M., Potokar, M., Kreft, M., Kralj-Iglic,
1121 V., Iglic, A., and Zorec, R. (2010). Fusion pore stability of peptidergic vesicles. Mol Membr
1122 Biol *27*, 65-80.

1123 Jorgacevski, J., Potokar, M., Grilc, S., Kreft, M., Liu, W., Barclay, J.W., Buckers, J., Medda,
1124 R., Hell, S.W., Parpura, V.*, et al.* (2011). Munc18-1 tuning of vesicle merger and fusion pore
1125 properties. J Neurosci *31*, 9055-9066.

1126 Julicher, F., and Lipowsky, R. (1996). Shape transformations of vesicles with intramembrane
1127 domains. Phys Rev E Stat Phys Plasmas Fluids Relat Interdiscip Topics *53*, 2670-2683.

1128 Julicher, F., and Seifert, U. (1994). Shape equations for axisymmetric vesicles: A
1129 clarification. Phys Rev E Stat Phys Plasmas Fluids Relat Interdiscip Topics *49*, 4728-4731.

1130 Kapur, J.N., Sahoo, P.K., and Wong, A.K.C. (1985). A New Method for Gray-Level Picture
1131 Thresholding Using the Entropy of the Histogram. Computer Vision Graphics and Image
1132 Processing *29*, 273-285.

1133 Khan, M., and Gasser, S. (2016). Generating Primary Fibroblast Cultures from Mouse Ear
1134 and Tail Tissues. J Vis Exp.

1135 Klyachko, V.A., and Jackson, M.B. (2002). Capacitance steps and fusion pores of small and
1136 large-dense-core vesicles in nerve terminals. Nature *418*, 89-92.

1137 Kreft, M., Jorgacevski, J., Stenovec, M., and Zorec, R. (2018). Angstrom-size exocytotic
1138 fusion pore: Implications for pituitary hormone secretion. Mol Cell Endocrinol *463*, 65-71.

1139 Kreft, M., Stenovec, M., Rupnik, M., Grilc, S., Krzan, M., Potokar, M., Pangrsic, T., Haydon,
1140 P.G., and Zorec, R. (2004). Properties of Ca(2+)-dependent exocytosis in cultured
1141 astrocytes. Glia *46*, 437-445.

1142 Krzan, M., Stenovec, M., Kreft, M., Pangrsic, T., Grilc, S., Haydon, P.G., and Zorec, R.
1143 (2003). Calcium-dependent exocytosis of atrial natriuretic peptide from astrocytes. J
1144 Neurosci *23*, 1580-1583.

1145 Kuchel, P.W., and Ralston, B.G. (1988). Theory and Problems of Biochemistry, Vol 7 (New
1146 York Schaum's Outline/McGraw-Hill).

1147 Lasic, E., Lisjak, M., Horvat, A., Bozic, M., Sakanovic, A., Anderluh, G., Verkhratsky, A.,
1148 Vardjan, N., Jorgacevski, J., Stenovec, M.*, et al.* (2019). Astrocyte Specific Remodeling of
1149 Plasmalemmal Cholesterol Composition by Ketamine Indicates a New Mechanism of
1150 Antidepressant Action. Sci Rep *9*, 10957.
1151 Lasic, E., Rituper, B., Jorgacevski, J., Kreft, M., Stenovec, M., and Zorec, R. (2016).
1152 Subanesthetic doses of ketamine stabilize the fusion pore in a narrow flickering state in
1153 astrocytes. J Neurochem *138*, 909-917.
1154 Levitan, I., Fang, Y., Rosenhouse-Dantsker, A., and Romanenko, V. (2010). Cholesterol and
1155 ion channels. Subcell Biochem *51*, 509-549.
1156 Li, N., Lee, B., Liu, R.J., Banasr, M., Dwyer, J.M., Iwata, M., Li, X.Y., Aghajanian, G., and
1157 Duman, R.S. (2010). mTOR-dependent synapse formation underlies the rapid
1158 antidepressant effects of NMDA antagonists. Science *329*, 959-964.
1159 Liscum, L. (2000). Niemann-Pick type C mutations cause lipid traffic jam. Traffic *1*, 218-225.
1160 Loftus, S.K., Morris, J.A., Carstea, E.D., Gu, J.Z., Cummings, C., Brown, A., Ellison, J.,
1161 Ohno, K., Rosenfeld, M.A., Tagle, D.A.*, et al.* (1997). Murine model of Niemann-Pick C
1162 disease: mutation in a cholesterol homeostasis gene. Science *277*, 232-235.
1163 Lollike, K., Borregaard, N., and Lindau, M. (1995). The exocytotic fusion pore of small
1164 granules has a conductance similar to an ion channel. J Cell Biol *129*, 99-104.
1165 Lollike, K., and Lindau, M. (1999). Membrane capacitance techniques to monitor granule
1166 exocytosis in neutrophils. J Immunol Methods *232*, 111-120.
1167 Maekawa, M. (2017). Domain 4 (D4) of Perfringolysin O to Visualize Cholesterol in Cellular
1168 Membranes-The Update. Sensors (Basel) *17*.
1169 Mahadeo, M., Furber, K.L., Lam, S., Coorssen, J.R., and Prenner, E.J. (2015). Secretory
1170 vesicle cholesterol: Correlating lipid domain organization and Ca2+ triggered fusion. Biochim
1171 Biophys Acta *1848*, 1165-1174.
1172 Mason, W.T., Rawlings, S.R., Cobbett, P., Sikdar, S.K., Zorec, R., Akerman, S.N., Benham,
1173 C.D., Berridge, M.J., Cheek, T., and Moreton, R.B. (1988). Control of secretion in anterior
1174 pituitary cells--linking ion channels, messengers and exocytosis. J Exp Biol *139*, 287-316.
1175 Mukherjee, S., and Maxfield, F.R. (2004). Lipid and cholesterol trafficking in NPC. Biochim
1176 Biophys Acta *1685*, 28-37.
1177 Mukherjee, S., Soe, T.T., and Maxfield, F.R. (1999). Endocytic sorting of lipid analogues
1178 differing solely in the chemistry of their hydrophobic tails. J Cell Biol *144*, 1271-1284.
1179 Najafinobar, N., Mellander, L.J., Kurczy, M.E., Dunevall, J., Angerer, T.B., Fletcher, J.S., and
1180 Cans, A.S. (2016). Cholesterol Alters the Dynamics of Release in Protein Independent Cell
1181 Models for Exocytosis. Sci Rep *6*, 33702.
1182 Nanavati, C., Markin, V.S., Oberhauser, A.F., and Fernandez, J.M. (1992). The exocytotic
1183 fusion pore modeled as a lipidic pore. Biophys J *63*, 1118-1132.
1184 Neher, E., and Marty, A. (1982). Discrete changes of cell membrane capacitance observed
1185 under conditions of enhanced secretion in bovine adrenal chromaffin cells. Proc Natl Acad
1186 Sci U S A *79*, 6712-6716.
1187 Ohno-Iwashita, Y., Iwamoto, M., Ando, S., Mitsui, K., and Iwashita, S. (1990). A modified
1188 theta-toxin produced by limited proteolysis and methylation: a probe for the functional study
1189 of membrane cholesterol. Biochim Biophys Acta *1023*, 441-448.
1190 Rand, R.P., and Parsegian, V.A. (1986). Mimicry and mechanism in phospholipid models of
1191 membrane fusion. Annu Rev Physiol *48*, 201-212.
1192 Rawicz, W., Olbrich, K.C., McIntosh, T., Needham, D., and Evans, E. (2000). Effect of chain
1193 length and unsaturation on elasticity of lipid bilayers. Biophys J *79*, 328-339.
1194 Ridler, T.W., and Calvard, S. (1978). Picture Thresholding Using an Iterative Selection
1195 Method. Ieee Transactions on Systems Man and Cybernetics *8*, 630-632.
1196 Rituper, B., Chowdhury, H.H., Jorgacevski, J., Coorssen, J.R., Kreft, M., and Zorec, R.
1197 (2013a). Cholesterol-mediated membrane surface area dynamics in neuroendocrine cells.
1198 Biochim Biophys Acta *1831*, 1228-1238.
1199 Rituper, B., Flašker, A., Guček, A., Chowdhury, H.H., and Zorec, R. (2012). Cholesterol and
1200 regulated exocytosis: A requirement for unitary exocytotic events. Cell Calcium *52*, 250-258.

1201 Rituper, B., Gucek, A., Jorgacevski, J., Flasker, A., Kreft, M., and Zorec, R. (2013b). High-
1202 resolution membrane capacitance measurements for the study of exocytosis and
1203 endocytosis. Nat Protoc *8*, 1169-1183.
1204 Rogasevskaia, T., and Coorssen, J.R. (2006). Sphingomyelin-enriched microdomains define
1205 the efficiency of native Ca(2+)-triggered membrane fusion. J Cell Sci *119*, 2688-2694.
1206 Sanacora, G., Treccani, G., and Popoli, M. (2012). Towards a glutamate hypothesis of
1207 depression: an emerging frontier of neuropsychopharmacology for mood disorders.
1208 Neuropharmacology *62*, 63-77.
1209 Schwartz, J.P., and Wilson, D.J. (1992). Preparation and characterization of type 1
1210 astrocytes cultured from adult rat cortex, cerebellum, and striatum. Glia *5*, 75-80.
1211 Seifert, U., Berndl, K., and Lipowsky, R. (1991). Shape transformations of vesicles: Phase
1212 diagram for spontaneous- curvature and bilayer-coupling models. Phys Rev A *44*, 1182-
1213 1202.
1214 Sharma, S., and Lindau, M. (2018). The fusion pore, 60 years after the first cartoon. FEBS
1215 Lett.
1216 Shin, W., Arpino, G., Thiyagarajan, S., Su, R., Ge, L., McDargh, Z., Guo, X., Wei, L.,
1217 Shupliakov, O., Jin, A.*, et al.* (2020). Vesicle Shrinking and Enlargement Play Opposing
1218 Roles in the Release of Exocytotic Contents. Cell Rep *30*, 421-431 e427.
1219 Shin, W., Ge, L., Arpino, G., Villarreal, S.A., Hamid, E., Liu, H., Zhao, W.D., Wen, P.J.,
1220 Chiang, H.C., and Wu, L.G. (2018). Visualization of Membrane Pore in Live Cells Reveals a
1221 Dynamic-Pore Theory Governing Fusion and Endocytosis. Cell *173*, 934-945 e912.
1222 Sikdar, S.K., Zorec, R., Brown, D., and Mason, W.T. (1989). Dual effects of G-protein
1223 activation on Ca-dependent exocytosis in bovine lactotrophs. FEBS Lett *253*, 88-92.
1224 Skocaj, M., Resnik, N., Grundner, M., Ota, K., Rojko, N., Hodnik, V., Anderluh, G., Sobota,
1225 A., Macek, P., Veranic, P.*, et al.* (2014). Tracking cholesterol/sphingomyelin-rich membrane
1226 domains with the ostreolysin A-mCherry protein. PLoS One *9*, e92783.
1227 Spruce, A.E., Breckenridge, L.J., Lee, A.K., and Almers, W. (1990). Properties of the fusion
1228 pore that forms during exocytosis of a mast cell secretory vesicle. Neuron *4*, 643-654.
1229 Stenovec, M., Kreft, M., Grilc, S., Pangrsic, T., and Zorec, R. (2008). EAAT2 density at the
1230 astrocyte plasma membrane and Ca(2 +)-regulated exocytosis. Mol Membr Biol *25*, 203-
1231 215.
1232 Stenovec, M., Kreft, M., Poberaj, I., Betz, W.J., and Zorec, R. (2004). Slow spontaneous
1233 secretion from single large dense-core vesicles monitored in neuroendocrine cells. FASEB J
1234 *18*, 1270-1272.
1235 Stenovec, M., Lasic, E., Bozic, M., Bobnar, S.T., Stout, R.F., Jr., Grubisic, V., Parpura, V.,
1236 and Zorec, R. (2016). Ketamine Inhibits ATP-Evoked Exocytotic Release of Brain-Derived
1237 Neurotrophic Factor from Vesicles in Cultured Rat Astrocytes. Mol Neurobiol *53*, 6882-6896.
1238 Stenovec, M., Trkov, S., Kreft, M., and Zorec, R. (2014). Alterations of calcium homoeostasis
1239 in cultured rat astrocytes evoked by bioactive sphingolipids. Acta Physiol (Oxf) *212*, 49-61.
1240 Stratton, B.S., Warner, J.M., Wu, Z., Nikolaus, J., Wei, G., Wagnon, E., Baddeley, D.,
1241 Karatekin, E., and O'Shaughnessy, B. (2016). Cholesterol Increases the Openness of
1242 SNARE-Mediated Flickering Fusion Pores. Biophys J *110*, 1538-1550.
1243 Svetina, S., and Zeks, B. (1989). Membrane bending energy and shape determination of
1244 phospholipid vesicles and red blood cells. Eur Biophys J *17*, 101-111.
1245 Tian, A., and Baumgart, T. (2009). Sorting of lipids and proteins in membrane curvature
1246 gradients. Biophys J *96*, 2676-2688.
1247 Trkov, S., Stenovec, M., Kreft, M., Potokar, M., Parpura, V., Davletov, B., and Zorec, R.
1248 (2012). Fingolimod--a sphingosine-like molecule inhibits vesicle mobility and secretion in
1249 astrocytes. Glia *60*, 1406-1416.
1250 Tsai, W.-H. (1995). Moment-preserving thresholding: a new approach. In Document image
1251 analysis, O.G. Lawrence, and K. Rangachar, eds. (IEEE Computer Society Press), pp. 44-
1252 60.
1253 Vardjan, N., Stenovec, M., Jorgacevski, J., Kreft, M., and Zorec, R. (2007). Subnanometer
1254 fusion pores in spontaneous exocytosis of peptidergic vesicles. J Neurosci *27*, 4737-4746.

Wang, N., Kwan, C., Gong, X., de Chaves, E.P., Tse, A., and Tse, F.W. (2010). Influence of cholesterol on catecholamine release from the fusion pore of large dense core chromaffin granules. J Neurosci *30*, 3904-3911.

Wasser, C.R., Ertunc, M., Liu, X., and Kavalali, E.T. (2007). Cholesterol-dependent balance between evoked and spontaneous synaptic vesicle recycling. J Physiol *579*, 413-429.

Winkler, M.B.L., Kidmose, R.T., Szomek, M., Thaysen, K., Rawson, S., Muench, S.P., Wustner, D., and Pedersen, B.P. (2019). Structural Insight into Eukaryotic Sterol Transport through Niemann-Pick Type C Proteins. Cell *179*, 485-497 e418.

Wustner, D., and Solanko, K. (2015). How cholesterol interacts with proteins and lipids during its intracellular transport. Biochim Biophys Acta *1848*, 1908-1926.

Xu, Y., Toomre, D.K., Bogan, J.S., and Hao, M. (2017). Excess cholesterol inhibits glucose-stimulated fusion pore dynamics in insulin exocytosis. J Cell Mol Med *21*, 2950-2962.

Yesylevskyy, S.O., Rivel, T., and Ramseyer, C. (2017). The influence of curvature on the properties of the plasma membrane. Insights from atomistic molecular dynamics simulations. Sci Rep *7*, 16078.

Zorec, R., Sikdar, S.K., and Mason, W.T. (1991). Increased cytosolic calcium stimulates exocytosis in bovine lactotrophs. Direct evidence from changes in membrane capacitance. J Gen Physiol *97*, 473-497.